Acta Geologica Sinica (English Edition), 2019, 93(5): 1500–1521

Geochronology and Geochemistry of Early Cretaceous Granitic Plutons in the Xing'an Massif, Great Xing'an Range, NE China: Petrogenesis and Tectonic Implications

DONG Yu[1, 2], GE Wenchun[1, 2, *], TIAN Dexin[3], JI Zheng[1, 2], YANG Hao[1, 2], BI Junhui[4], WU Haoran[1, 2] and HAO Yujie[1, 2]

[1] *College of Earth Sciences, Jilin University, Changchun 130061, China*
[2] *Key Laboratory of Mineral Resources Evaluation in Northeast Asia, Ministry of Natural Resources, Changchun 130061, China*
[3] *Nonferrous Metals Geological Exploration Bureau of Zhejiang Province, Shaoxing, Zhejiang 312000, China*
[4] *Tianjin Center, China Geological Survey, Tianjin 300170, China*

Abstract: In this study, we present zircon U-Pb ages, whole-rock geochemical data and Hf isotopic compositions for the Meiguifeng and Arxan plutons in Xing'an Massif, Great Xing'an Range, which can provide important information in deciphering both Mesozoic magmatism and tectonic evolution of NE China. The zircon U-Pb dating results indicate that alkali feldspar granite from Meiguifeng pluton was emplaced at ~145 to 137 Ma, and granite porphyry of Arxan pluton was formed at ~129 Ma. The Meiguifeng and Arxan plutons have similar geochemical features, which are characterized by high silica, total alkalis, differentiation index, with low P_2O_5, CaO, MgO, TFe_2O_3 contents. They belong to high-K calc-alkaline series, and show weakly peraluminous characteristics. The Meiguifeng and Arxan plutons are both enriched in LREEs and LILEs (e.g., Rb, Th, U and K), and depleted in HREEs and HFSEs (e.g., Nb, Ta and Ti). Combined with the petrological and geochemical features, the Meiguifeng and Arxan plutons show highly fractionated I-type granite affinity. Moreover, the Meiguifeng and Arxan plutons may share a common or similar magma source, and they were probably generated by partial melting of Neoproterozoic high-K basaltic crust. Meanwhile, plagioclase, K-feldspar, biotite, apatite, monazite, allanite and Ti-bearing phases fractionated from the magma during formation of Meiguifeng and Arxan plutons. Combined with spatial distribution and temporal evolution, we assume that the generation of Early Cretaceous Meiguifeng and Arxan plutons in Great Xing'an Range was closely related to the break-off of Mudanjiang oceanic plate. Furthermore, the Mudanjiang Ocean was probably a branch of Paleo-Pacific Ocean.

Key words: geochemistry, geochronology, Early Cretaceous, highly fractionated I-type granite, Great Xing'an Range

Citation: Dong et al., 2019. Geochronology and Geochemistry of Early Cretaceous Granitic Plutons in the Xing'an Massif, Great Xing'an Range, NE China: Petrogenesis and Tectonic Implications. Acta Geologica Sinica (English Edition), 93(5): 1500–1521. DOI: 10.1111/1755-6724.14391

1 Introduction

The Central Asian Orogenic Belt (CAOB) is the most important accretionary orogenic belt in the world, which developed during the Neoproterozoic to Phanerozoic between Siberian and East European cratons in the north and North China and Tarim cratons in the south, occupying an immense range of China, Russia, Mongolia, Kazakhstan and surrounding areas (Fig. 1a; Jahn et al., 2000, 2004, 2009; Badarch et al., 2000; Li, 2006; Cai et al., 2012; Safonova and Santosh, 2014; Xiao and Santosh, 2014). NE China is the easternmost part of CAOB, and it is characterized by abundant granitoid, exposed over an area of about 200,000 km^2 (Wu et al., 2011). For the past decade, precise geochronological work has been done in NE China, which is marked by large scale Mesozoic magmatism, forming a key part of Mesozoic magmatic belt in CAOB (Wu et al., 2002, 2011, 2015; Ge et al., 2005; Cheng et al., 2006; Zhang et al., 2008, 2018; Wilde et al., 2010; She et al., 2012; Wang et al., 2012a, b, 2015, 2019; Gao et al., 2013; Shi et al., 2013, 2015; Yu et al., 2013a, b; Li et al., 2014, 2015a, b, 2018a, b; Bi et al., 2015; Chen et al., 2015; Tian et al., 2015; Dong et al., 2016a; Ji et al., 2016a, b, 2018a, 2019; He et al., 2017, 2018; Xie et al., 2017; Xu et al., 2018; Yin et al., 2018). However, its geodynamic mechanism and evolution still remain controversial (Zhang et al., 2010a, b; Wu et al., 2011; She et al., 2012; Wang et al., 2012a, b, 2015; Shi et al., 2013, 2015; Xu et al., 2013a, b; Tian et al., 2015; Dong et al., 2014, 2016a, b; Li et al., 2014, 2015a, b, 2018a, b; Tang et al., 2014, 2016; Ji et al., 2016a, b, 2018a, 2019; He et al., 2017, 2018; Xie et al., 2017). Unlike other areas in CAOB, NE China can be thought of as one of the important areas of eastern Asian active continental margin, and therefore it was commonly considered that the tectonic evolution of NE China was controlled by the Paleo-Pacific tectonic regime (Zhang et al., 2010a, b; Tian et al., 2015; Dong et al., 2014, 2016a, b;

* Corresponding author. E-mail: gewenchun@jlu.edu.cn

http://www.geojournals.cn/dzxbcn/ch/index.aspx; https://onlinelibrary.wiley.com/journal/17556724

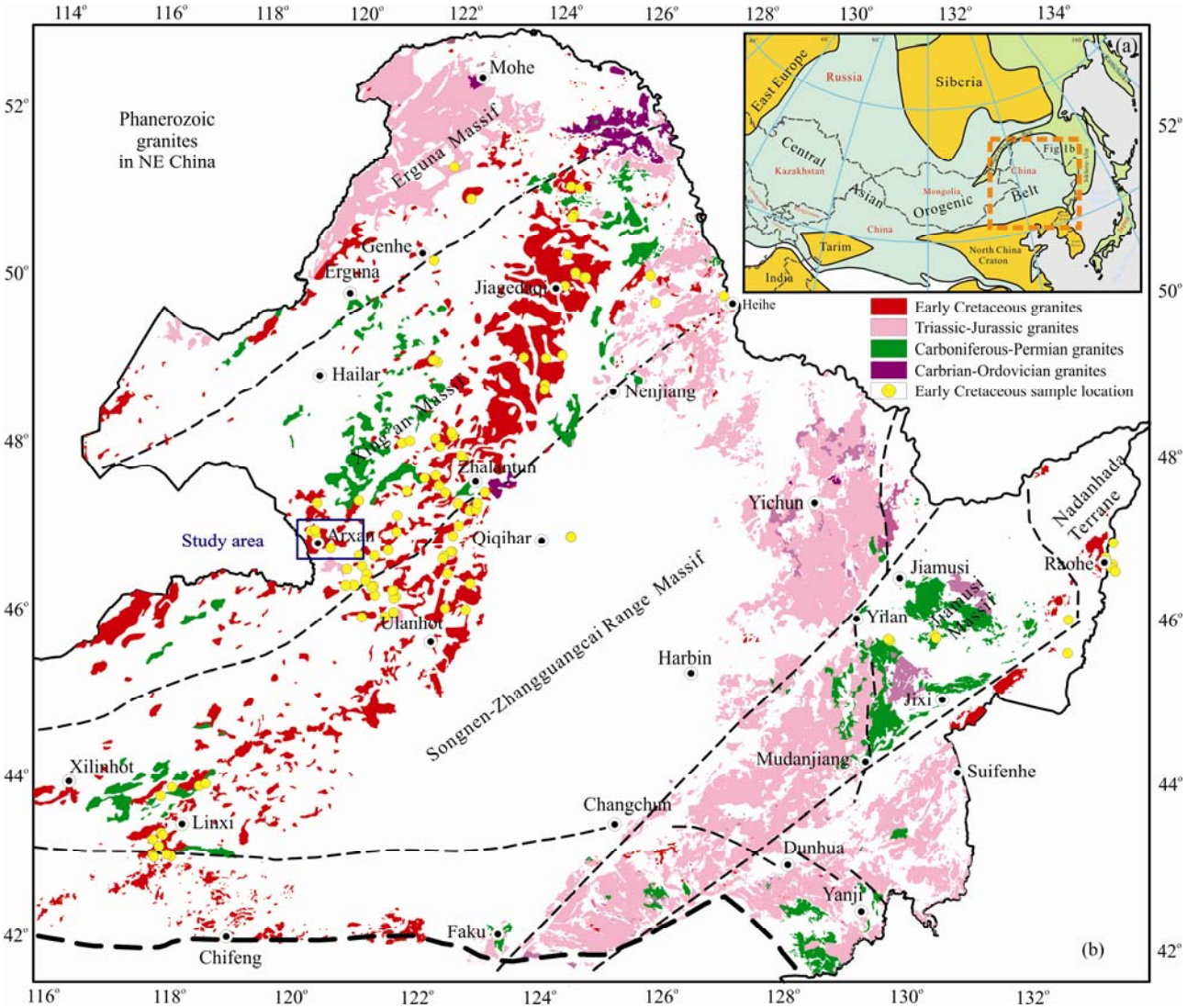

Fig. 1. (a) General map showing the location of Central and East Asia, after Safonova and Santosh (2014); (b) distribution of granitic rocks in NE China (showing sampling locations of Early Cretaceous granitic rocks collected in this study) and simplified tectonic subdivisions of NE China.

He et al., 2017, 2018; Xie et al., 2017). In the past decade, some studies have suggested that a double-side subduction is favored for the tectonic evolution of Mongol-Okhotsk Ocean, and the Mongol-Okhotsk tectonic regime probably plays an important role in the Mesozoic magmatism and tectonic evolution in NE China (Wang et al., 2012a, 2015; Li et al., 2014, 2015a, b, 2018a, b; Tang et al., 2014, 2016; Ji et al., 2016a, b, 2018a, 2019). Therefore, and the deep geodynamic background of Mesozoic igneous rocks in NE China remains unclear. NE China might have undergone combined effect of the Paleo-Pacific and Mongol-Okhotsk tectonic regimes, implying a complex tectonic evolutionary history (Zhang et al., 2010a, b; Wu et al., 2011; She et al., 2012; Wang et al., 2012a, b, 2015; Shi et al., 2013, 2015; Xu et al., 2013a, b; Tian et al., 2015; Dong et al., 2014, 2016a, b; Li et al., 2014, 2015a, b, 2018a, b; Tang et al., 2014, 2016; Ji et al., 2016a, b, 2018a, 2019; He et al., 2017, 2018; Xie et al., 2017). Thus, one question can be posed: which regime was predominantly responsible for the Mesozoic magmatism and tectonic evolution in NE China?

The Great Xing'an Range is characterized by large volumes of Mesozoic granitoid and volcanic rock, and Early Cretaceous was a significant period of magmatism in the Great Xing'an Range (Wu et al., 2002, 2011, 2015; Ge et al., 2005; Zhang et al., 2008, 2018; She et al., 2012; Wang et al., 2012b, 2019; Gao et al., 2013; Shi et al., 2013, 2015; Chen et al., 2015; Li et al., 2015b, 2018a, b; Tian et al., 2015; Ji et al., 2016a, b, 2018a, 2019; He et al., 2017, 2018; Xie et al., 2017; Xu et al., 2018; Yin et al., 2018). Therefore, Early Cretaceous granitoid in the Great Xing'an Range becomes an important research object. Here, we present zircon U-Pb ages, whole-rock geochemical data and Hf isotopic compositions for the Meiguifeng and Arxan plutons in Xing'an Massif, Great Xing'an Range (Fig. 1b). These data, combined with previous researches on coeval magma-tectonic event in NE China, not only constrain the temporal-spatial

distribution, petrogenesis and source of Early Cretaceous granitoid, but also provide important information in revealing the geodynamic mechanism of Early Cretaceous magmatism in NE China.

2 Geological Setting and Sample Descriptions

NE China is composed of a collage of microcontinental massifs, including the Erguna Massif to the northwest, Xing'an and Songnen-Zhangguangcai Range massifs to the central, and Jiamusi Massif and Nadanhada Terrane to the east (Fig. 1b). During the Paleozoic, NE China was controlled by the Paleo-Asian oceanic tectonic regime, and the closure of Paleo-Asian Ocean has resulted in the amalgamation of Erguna, Xing'an and Songnen-Zhangguangcai Range massifs (Wu et al., 2011; Yu et al., 2014, 2017; Dong et al., 2016c; Liu et al., 2017; Ji et al., 2018b). In the Mesozoic, NE China experienced the subduction of Paleo-Pacific Ocean and closure of Mongol-Okhotsk Ocean, which caused the formation of immense volumes of granitoid and volcanic rock, together with the amalgamation of Jiamusi Massif and Nadanhada Terrane (Wu et al., 2002, 2011, 2015; Ge et al., 2005; Cheng et al., 2006; Zhang et al., 2008, 2018; Wilde et al., 2010; She et al., 2012; Wang et al., 2012b, 2019; Gao et al., 2013; Shi et al., 2013, 2015; Yu et al., 2013a, b; Li et al., 2014, 2015a, b, 2018a, b; Bi et al., 2015; Chen et al., 2015; Tian et al., 2015; Dong et al., 2016a; Ji et al., 2016a, b, 2018, 2019; He et al., 2017, 2018; Xie et al., 2017; Dong et al., 2018, 2019; Xu et al., 2018; Yin et al., 2018).

The Xing'an Massif, located in the Great Xing'an Range, was previously considered to contain Precambrian metamorphic basement materials (IMBGMR, 1991). However, recent geochronological data have suggested that they are re-interpreted as Late-Paleozoic to Early Mesozoic metamorphic complexes (Miao et al., 2004, 2007). The Xing'an Massif has undergone multiple magma-tectonic activities since the Paleozoic time (Wu et al., 2002, 2011, 2015; Ge et al., 2005; Zhang et al., 2008, 2018; Zhao, 2011; She et al., 2012; Wang et al., 2012b, 2019; Gao et al., 2013; Shi et al., 2013, 2015; Chen et al., 2015; Li et al., 2018a, b; Tian et al., 2015; Dong et al., 2014, 2016b, c; Ji et al., 2016a, b, 2018a, b, 2019; He et al., 2017, 2018; Liu et al., 2017; Xie et al., 2017; Yu, 2017; Xu et al., 2018; Yin et al., 2018). The Ordovician-Silurian (~480–420 Ma) magmatic arcs have been identified in the Xing'an Massif (Liu et al., 2017; Ji et al., 2018b). The Late Paleozoic magmatism mainly took place in the Early Carboniferous to Middle Permian (~360–260 Ma), which elongate in a NE-SW orientation from Dongwuqi through the area around Arxan and Wuerqihan to Nenjiang (Zhao, 2011; Wu et al., 2011; Dong et al., 2016c; Liu et al., 2017; Yu, 2017; Ji et al., 2018b). It is noteworthy that the Mesozoic igneous rocks are widely distributed in Xing'an Massif, which are mainly granitic intrusive rocks and intermediate-acidic volcanic rocks (Wu et al., 2002, 2011, 2015; Ge et al., 2005; Zhang et al., 2008, 2018; She et al., 2012; Wang et al., 2012b, 2019; Gao et al., 2013; Shi et al., 2013, 2015; Chen et al., 2015; Li et al., 2018a, b; Tian et al., 2015; Dong et al., 2014, 2016b; Ji et al., 2016a, b, 2018a, 2019; He et al., 2017, 2018; Liu et al., 2017; Xie et al., 2017; Xu et al., 2018; Yin et al., 2018).

This study focuses on two granitic plutons within the Xing'an Massif, namely Meiguifeng (samples 13GW405, 13GW406, 13GW420, 13GW421, 13GW422, 13GW423 and 13GW425) and Arxan plutons (samples GW04209, GW04210, GW04211, GW04212, GW04213), which were chosen for geochronological and geochemical analyses. Due to the dense forests in Great Xing'an Range, the geological boundaries between the geological bodies couldn't be exactly determined (Fig. 2).

The Meiguifeng pluton, located near the Meiguifeng-Shuqiu area, Arxan City, is dominated by alkali feldspar granite (Fig. 3a). The Meiguifeng pluton intrudes the Late Paleozoic strata, and is overlain by the Cenozoic sediments (Fig. 2). The alkali feldspar granite from Meiguifeng pluton shows a miarolitic texture and a massive structure, which consists of alkali feldspar, quartz and plagioclase, with minor hornblende and accessory zircon and apatite (Fig. 3b and 3c).

The Arxan pluton, located near the highest region of Arxan Mountain, intrudes the Late Paleozoic strata, and is overlain by the Cenozoic sediments (Fig. 2). The Arxan pluton is composed of granite porphyry, with a porphyritic texture and a massive structure. The phenocryst is mainly alkali feldspar, and the main rock-forming minerals are alkali feldspar, quartz, plagioclase and hornblende, with accessory zircon and apatite (Fig. 3d).

3 Analytical Methods

3.1 Zircon U-Pb dating

Zircon grains for U-Pb dating were separated by combining heavy liquid and magnetic techniques, and then by handpicking under a binocular microscope at the Langfang Regional Geological Survey, Hebei Province. Zircon internal structures were examined under transmitted and reflected light micrographs as well as cathodoluminescence (CL) images. Zircon grains of euhedral, transparent, unfractured and inclusion-free zircons were chosen for U-Pb dating. The zircon U-Pb isotopic analyses were completed in two laboratories. Samples 13GW405, 13GW420, 13GW425 were conducted using an Agilent 7500 inductively coupled plasma mass spectrometer (ICP-MS) equipped with a 193nm laser ablation system (LA) in the Institute of Geology and Geophysics, Chinese Academy of Sciences in Beijing, with a laser spot of 36 μm, ablation time of 45 s and ablation rate of 10Hz. Zircon grains from sample GW04209 were dated on the ELAN 6100 ICP-MS connected with a 193 nm ArF-excimer LA system at the State Key Laboratory of Continental Dynamics, Northwest University, China, with a laser spot of 30 μm. Zircon 91500 was applied to be external standard for age calibration, and the NIST SRM610 was used for the instrument optimization. Isotopic ratios and element concentrations were calculated using the Glitter program (ver.4.4, Macquarie University). The ages were calculated using Isoplot (ver 3.0) (Ludwig, 2003). The common Pb was corrected following Andersen (2002). Age uncertainties are quoted at the 95% (2σ) confidence level.

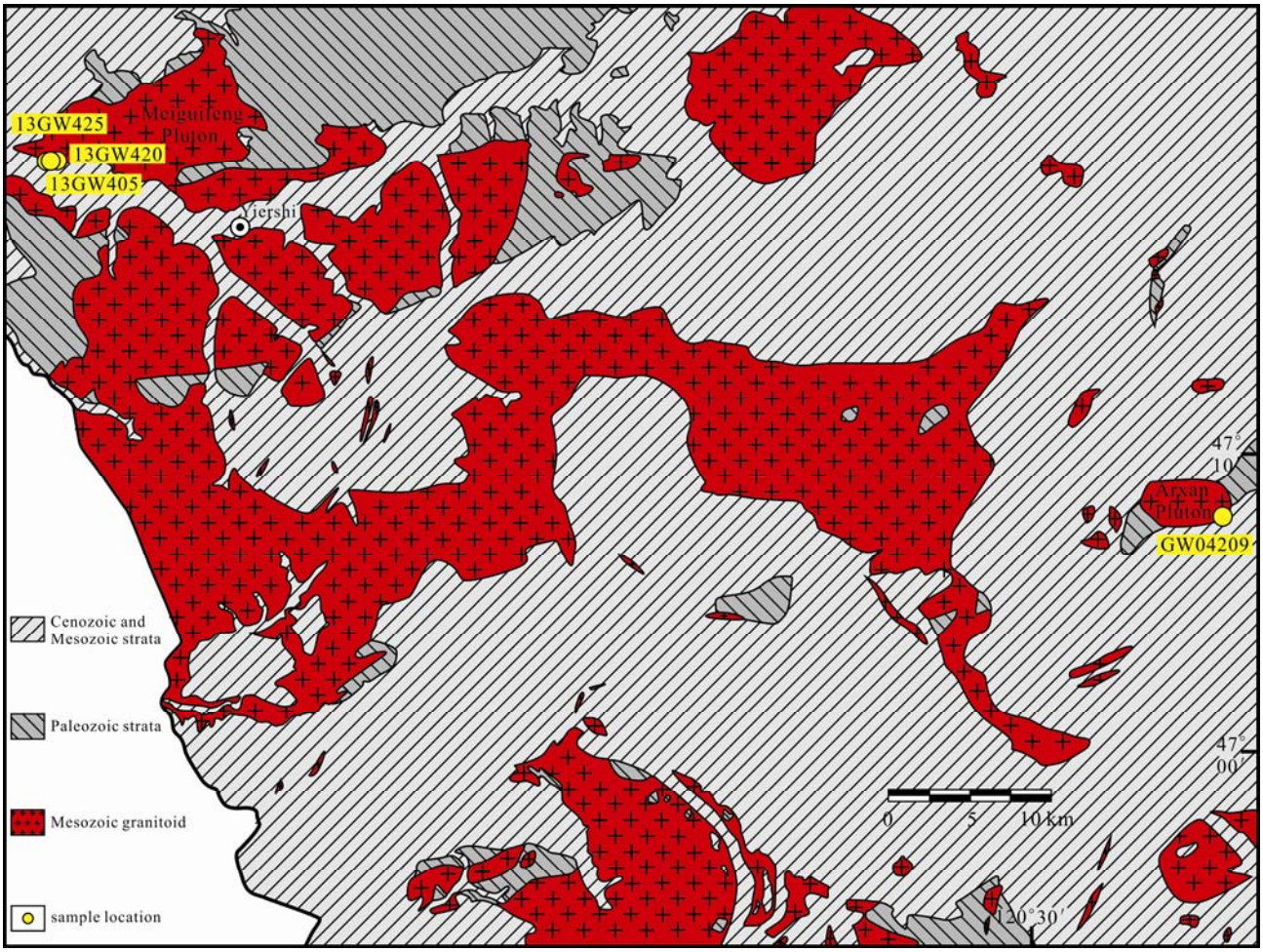

Fig. 2. Detailed geological map of the study area in Great Xing'an Range, showing sample locations.

3.2 Lu-Hf isotope analyses

In situ zircon Hf isotopic analyses of four dated samples (13GW405, 13GW420, 13GW425 and GW04209) were conducted using a Neptune MC-ICP-MS, equipped with a 193nm laser system, at the Institute of Geology and Geophysics, Chinese Academy of Sciences in Beijing, China. During the analyses, a laser repetition rate of 10 Hz at 100 mJ was used, with a spot size of 63 μm. The analytical procedures were described by Wu et al. (2006). Measured $^{176}Hf/^{177}Hf$ and $^{176}Lu/^{177}Hf$ ratios were adopted to calculate the initial $^{176}Hf/^{177}Hf$ ratios, taking a decay constant for ^{176}Lu as 1.865×10^{-11} year^{-1} (Scherer et al., 2001). The present-day chondritic ratios of $^{176}Hf/^{177}Hf$=0.282772 and $^{176}Lu/^{177}Hf$=0.0332 were used to calculate $\varepsilon_{Hf}(t)$ values (Blichert-Toft and Albarède, 1997). The calculation of two-stage model ages was based on the average crustal value of f_{cc}= –0.548 (Veevers et al., 2005).

3.3 Major and trace elemental analyses

The samples chosen for elemental analyses were crushed in an agate mill to ~200 mesh after the removal of altered surfaces. The whole-rock chemical analyses were completed in two laboratories. Samples 13GW405, 13GW406, 13GW420, 13GW421, 13GW422, 13GW423, and 13GW425 were finished at the Beijing Research Institute of Uranium Geology, China, and samples GW04209, GW04210, GW04211, GW04212, GW04213 were conducted at the State Key Laboratory of Continental Dynamics, Northwest University, China. Major and trace elemental compositions were analyzed by X-ray fluorescence (XRF) and ICP-MS, respectively. Analytical precisions were generally better than 1%–3% for major elements. For trace element analyses, analytical precisions were better than 2%, and the detection limits for most trace elements are better than 2 ppb.

4 Analytical Results

4.1 Zircon U-Pb ages and Hf isotopic compositions

In this study, four representative samples from Meiguifeng and Arxan plutons in the central Great Xing'an Range were chosen for zircon U-Pb-Hf isotopic analyses (Table 1 and 2). Zircon grains from these plutons are mostly euhedral-subhedral in shape, showing fine-scale oscillatory growth zoning (Fig. 4), with high Th/U ratios (0.26–1.89). All these characteristics imply their magmatic origin (Koschek, 1993; Pupin, 1980).

Sample 13GW405 (47°19′28.8″N, 119°41′25.6″E), 13GW420 (47°19′31.6″N, 119°41′46.4″E) and 13GW425

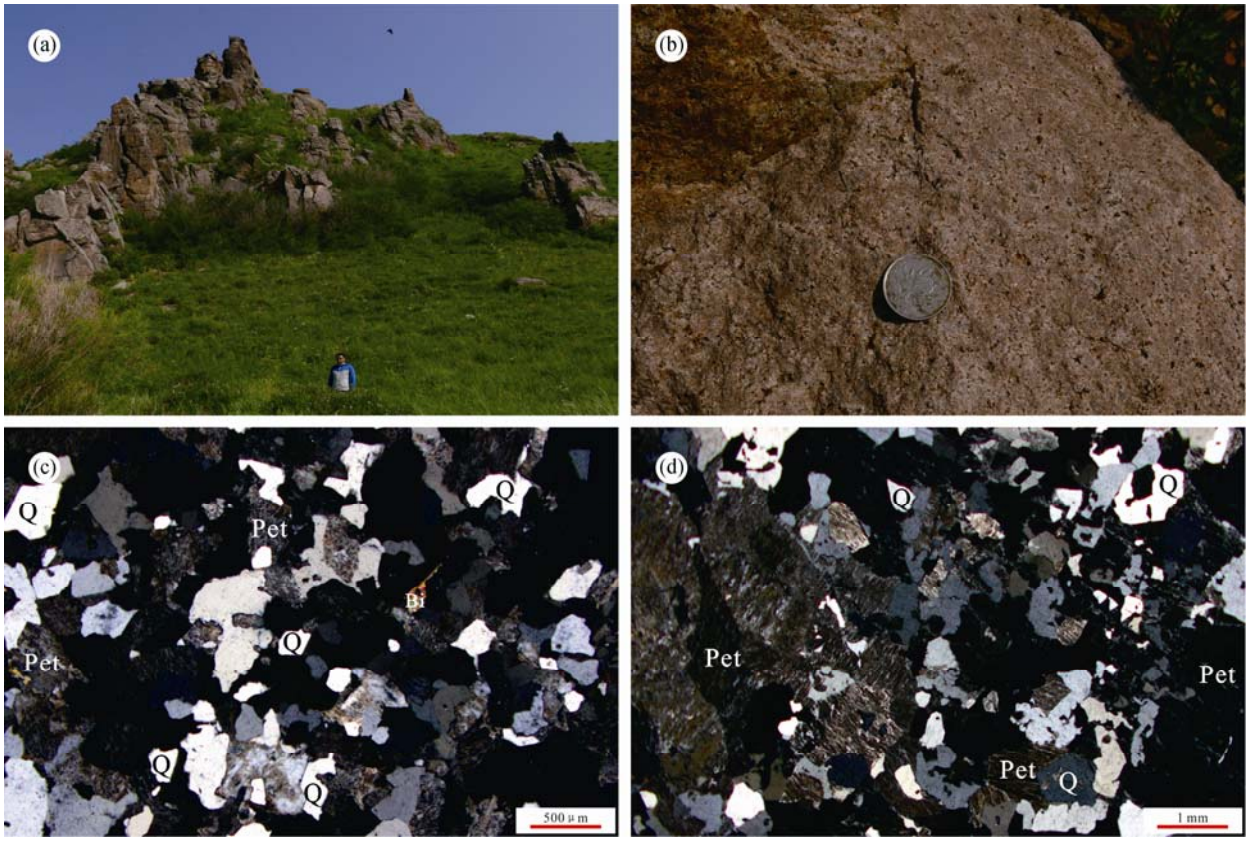

Fig. 3. Representative photographs and microphotographs of the Meiguifeng and Arxan plutons in Great Xing'an Range.
(a) Meiguifeng pluton; (b) alkali feldspar granite from Meiguifeng pluton; (c) alkali feldspar granite (sample 13GW406), cross polarized light; (d) granite porphyry (sample GW04209), cross polarized light. Abbreviations: Bi = biotite; Pet = perthite; Q = quartz.

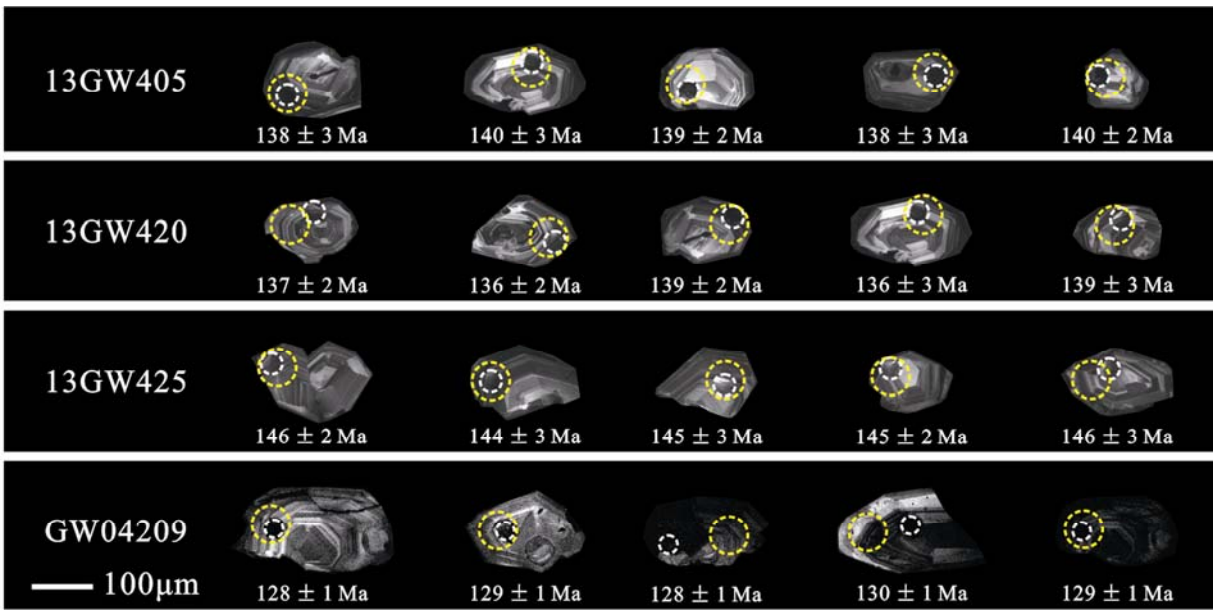

Fig. 4. Representative CL images of zircons from the Meiguifeng and Arxan plutons in Great Xing'an Range. White circles indicate the locations of LA-ICP-MS U-Pb analyses. Yellow circles show the locations of *in situ* zircon Hf isotopic analyses.

(47°19′28.8″N, 119°41′20.1″E), alkali feldspar granite, were both collected from the Meiguifeng pluton. The $^{206}Pb/^{238}U$ ages obtained from 24 analytical spots for 13GW405 range from 142 Ma to 136 Ma (Fig. 5a), and they give a weighted mean $^{206}Pb/^{238}U$ age of 139±1 Ma (MSWD=0.45, n=24). Twenty-five zircon grains were dated from 13GW420, and twenty-four analyzed spots yield a weighted mean $^{206}Pb/^{238}U$ age of 137 ± 1 Ma (Fig.

Table 1 LA-ICP-MS zircon U-Pb dating data for the granites from Meiguifeng and Arxan plutons in Great Xing'an Range

Sample no.	Th	U	Pb	Th/U	Isotopic ratios						Age (Ma)					
					$^{207}Pb/^{206}Pb$		$^{207}Pb/^{235}U$		$^{206}Pb/^{238}U$		$^{207}Pb/^{206}Pb$		$^{207}Pb/^{235}U$		$^{206}Pb/^{238}U$	
	ppm	ppm	ppm		Ratio	1σ	Ratio	1σ	Ratio	1σ	Ages	1σ	Age	1σ	Age	1σ
13GW405-01	103.52	118.16	11.44	0.88	0.04931	0.00500	0.14700	0.01456	0.02162	0.00055	163	175	139	13	138	3
13GW405-02	98.27	188.90	16.90	0.52	0.04884	0.00161	0.14984	0.00464	0.02225	0.00038	140	42	142	4	142	2
13GW405-03	147.80	263.28	23.30	0.56	0.05090	0.00235	0.15200	0.00669	0.02166	0.00041	236	67	144	6	138	3
13GW405-04	318.75	487.64	44.70	0.65	0.05005	0.00223	0.15303	0.00654	0.02218	0.00040	197	66	145	6	141	3
13GW405-05	104.56	202.72	17.93	0.52	0.04973	0.00720	0.15103	0.02148	0.02203	0.00068	182	256	143	19	140	4
13GW405-06	103.34	385.39	32.17	0.27	0.04932	0.00440	0.14554	0.01253	0.02140	0.00058	163	143	138	11	136	4
13GW405-07	145.10	364.62	31.56	0.40	0.04878	0.01300	0.14594	0.03849	0.02170	0.00087	137	399	138	34	138	5
13GW405-08	274.33	485.90	43.76	0.56	0.04923	0.00388	0.14706	0.01125	0.02166	0.00050	159	129	139	10	138	3
13GW405-09	60.98	123.90	10.88	0.49	0.04955	0.00225	0.14769	0.00639	0.02162	0.00041	174	66	140	6	138	3
13GW405-10	198.67	362.17	32.37	0.55	0.04919	0.00440	0.14598	0.01272	0.02152	0.00053	157	150	138	11	137	3
13GW405-11	110.04	283.54	24.30	0.39	0.04876	0.00187	0.14490	0.00526	0.02155	0.00039	136	52	137	5	137	2
13GW405-12	66.07	156.28	13.53	0.42	0.05072	0.00232	0.15170	0.00662	0.02169	0.00041	228	66	143	6	138	3
13GW405-13	350.19	457.64	42.03	0.77	0.05116	0.00437	0.15308	0.01267	0.02170	0.00055	248	141	145	11	138	3
13GW405-14	73.87	222.50	18.29	0.33	0.05062	0.00479	0.15025	0.01387	0.02153	0.00054	224	162	142	12	137	3
13GW405-15	431.13	632.09	57.43	0.68	0.04956	0.00350	0.15012	0.01029	0.02197	0.00047	174	116	142	9	140	3
13GW405-16	62.28	197.36	16.17	0.32	0.04984	0.00227	0.14849	0.00641	0.02161	0.00042	188	64	141	6	138	3
13GW405-17	103.72	260.88	22.24	0.40	0.04904	0.00433	0.14876	0.01280	0.02200	0.00053	150	148	141	11	140	3
13GW405-18	205.58	372.03	32.42	0.55	0.04994	0.00149	0.14802	0.00412	0.02150	0.00036	192	35	140	4	137	2
13GW405-19	71.27	192.04	16.15	0.37	0.05093	0.00688	0.15484	0.02057	0.02205	0.00061	238	245	146	18	141	4
13GW405-20	120.92	404.52	33.39	0.30	0.04947	0.00194	0.14962	0.00557	0.02193	0.00039	170	54	142	5	140	2
13GW405-21	76.89	186.67	15.80	0.41	0.05101	0.00138	0.15305	0.00382	0.02176	0.00036	241	61	145	3	139	2
13GW405-22	152.81	359.08	37.34	0.43	0.05073	0.00152	0.15274	0.00424	0.02184	0.00037	229	34	144	4	139	2
13GW405-23	77.36	301.26	24.21	0.26	0.04971	0.00197	0.15226	0.00574	0.02222	0.00039	181	55	144	5	142	2
13GW405-24	71.82	147.55	12.59	0.49	0.04877	0.00306	0.14487	0.00874	0.02154	0.00047	137	97	137	8	137	3
13GW420-01	140.99	170.58	4.46	0.83	0.04903	0.00308	0.14732	0.00914	0.02179	0.00045	149	103	140	8	139	3
13GW420-02	211.66	293.22	7.41	0.72	0.04885	0.00218	0.14576	0.00651	0.02164	0.00039	141	71	138	6	138	2
13GW420-03	386.85	273.59	8.02	1.41	0.04880	0.00272	0.14255	0.00788	0.02118	0.00042	138	89	135	7	135	3
13GW420-04	279.16	263.34	7.25	1.06	0.04884	0.00248	0.14709	0.00743	0.02184	0.00041	140	81	139	7	139	3
13GW420-05	253.68	300.11	7.82	0.85	0.04889	0.00227	0.14644	0.00680	0.02172	0.00039	143	75	139	6	139	2
13GW420-06	112.44	135.50	3.59	0.83	0.04890	0.00401	0.14736	0.01194	0.02185	0.00049	143	140	140	11	139	3
13GW420-07	96.88	92.16	2.49	1.05	0.04883	0.00616	0.14652	0.01833	0.02176	0.00053	140	232	139	16	139	3
13GW420-08	287.35	240.61	6.82	1.19	0.04916	0.00308	0.14778	0.00920	0.02180	0.00044	155	104	140	8	139	3
13GW420-09	219.90	352.34	8.78	0.62	0.04896	0.00203	0.14764	0.00612	0.02187	0.00040	146	63	140	5	139	3
13GW420-10	629.76	466.31	13.52	1.35	0.04886	0.00221	0.14484	0.00657	0.02150	0.00038	141	73	137	6	137	2
13GW420-11	176.11	190.24	5.03	0.93	0.04879	0.00400	0.14549	0.01184	0.02162	0.00045	138	143	138	10	138	3
13GW420-12	215.64	429.51	10.44	0.50	0.04894	0.00208	0.14870	0.00636	0.02203	0.00039	145	67	141	6	140	2
13GW420-13	186.30	192.93	5.09	0.97	0.04915	0.00360	0.14443	0.01048	0.02131	0.00045	155	124	137	9	136	3
13GW420-14	1170.77	620.97	19.53	1.89	0.04882	0.00160	0.14302	0.00478	0.02124	0.00036	139	47	136	4	135	2
13GW420-15	275.36	273.01	7.28	1.01	0.05019	0.00389	0.14753	0.01141	0.02132	0.00041	204	139	140	10	136	3
13GW420-16	273.63	364.40	9.17	0.75	0.04888	0.00260	0.14376	0.00766	0.02133	0.00039	142	88	136	7	136	2
13GW420-17	443.40	605.39	15.30	0.73	0.04887	0.00180	0.14503	0.00540	0.02152	0.00038	142	54	138	5	137	2
13GW420-18	517.59	396.19	12.05	1.31	0.04906	0.00252	0.15606	0.00801	0.02307	0.00042	151	84	147	7	147	3
13GW420-19	219.85	337.79	8.56	0.65	0.04902	0.00345	0.14934	0.01053	0.02209	0.00040	149	125	141	9	141	3
13GW420-20	199.80	258.33	6.60	0.77	0.04881	0.00317	0.14381	0.00926	0.02136	0.00042	139	108	136	8	136	3
13GW420-21	219.06	342.53	8.29	0.64	0.05016	0.00303	0.14488	0.00870	0.02095	0.00042	202	101	137	8	134	3
13GW420-22	347.64	249.22	7.26	1.39	0.04879	0.00225	0.14356	0.00660	0.02134	0.00040	138	72	136	6	136	3
13GW420-23	316.75	334.38	8.79	0.95	0.04885	0.00242	0.14369	0.00711	0.02133	0.00039	141	80	136	6	136	2
13GW420-24	353.47	571.07	13.96	0.62	0.04878	0.00193	0.14305	0.00572	0.02126	0.00036	137	62	136	5	136	2
13GW420-25	84.67	107.93	2.77	0.78	0.04892	0.00550	0.14678	0.01634	0.02176	0.00053	144	204	139	14	139	3
13GW425-01	102.96	273.62	6.58	0.38	0.04942	0.00247	0.15632	0.00786	0.02293	0.00041	168	84	147	7	146	3
13GW425-02	321.48	272.69	7.92	1.18	0.04951	0.00225	0.15655	0.00716	0.02293	0.00041	172	73	148	6	146	3
13GW425-03	368.13	406.14	11.13	0.91	0.04879	0.00167	0.15402	0.00536	0.02288	0.00039	138	50	145	5	146	2
13GW425-04	152.62	143.48	4.05	1.06	0.04877	0.00534	0.15187	0.01657	0.02258	0.00048	137	205	144	15	144	3
13GW425-05	101.60	116.14	3.19	0.87	0.04899	0.00374	0.15316	0.01151	0.02266	0.00052	147	126	145	10	144	3
13GW425-06	197.20	216.62	5.97	0.91	0.04951	0.00496	0.15415	0.01521	0.02257	0.00058	172	173	146	13	144	4
13GW425-07	248.69	250.99	6.86	0.99	0.04908	0.00265	0.15197	0.00819	0.02245	0.00042	152	89	144	7	143	3
13GW425-08	115.38	168.42	4.27	0.69	0.04875	0.00410	0.15021	0.01253	0.02234	0.00048	136	146	142	11	142	3
13GW425-09	143.18	207.28	5.41	0.69	0.04904	0.00288	0.15311	0.00895	0.02263	0.00043	150	98	145	8	144	3
13GW425-10	127.09	168.94	4.49	0.75	0.04907	0.00261	0.15522	0.00819	0.02293	0.00045	151	85	147	7	146	3
13GW425-11	687.59	412.13	13.35	1.67	0.04951	0.00180	0.15379	0.00568	0.02252	0.00039	172	54	145	5	144	2
13GW425-12	130.90	120.61	3.35	1.09	0.05010	0.00520	0.15436	0.01589	0.02234	0.00051	200	189	146	14	142	3
13GW425-13	542.81	363.92	11.20	1.49	0.04861	0.00227	0.15128	0.00710	0.02256	0.00040	129	75	143	6	144	3
13GW425-14	239.41	235.70	6.72	1.02	0.04888	0.00216	0.15531	0.00688	0.02304	0.00042	142	69	147	6	147	3
13GW425-15	311.22	296.62	8.23	1.05	0.05037	0.00253	0.15650	0.00794	0.02253	0.00039	212	85	148	7	144	2
13GW425-16	257.31	311.05	8.29	0.83	0.04888	0.00186	0.15385	0.00594	0.02282	0.00040	142	58	145	5	145	3
13GW425-17	173.36	211.72	5.76	0.82	0.04885	0.00200	0.15505	0.00639	0.02301	0.00041	141	63	146	6	147	3
13GW425-18	123.91	152.75	4.42	0.81	0.04941	0.00429	0.16750	0.01446	0.02458	0.00050	167	156	157	13	157	3
13GW425-19	96.63	122.54	3.26	0.79	0.04882	0.00354	0.15503	0.01114	0.02302	0.00048	139	123	146	10	147	3
13GW425-20	353.91	227.85	7.15	1.55	0.04893	0.00265	0.15443	0.00836	0.02288	0.00043	144	89	146	7	146	3
13GW425-21	189.72	257.85	6.79	0.74	0.04978	0.00260	0.15672	0.00820	0.02282	0.00042	185	87	148	7	145	3
13GW425-22	500.99	336.83	10.47	1.49	0.04993	0.00211	0.15676	0.00669	0.02276	0.00039	192	67	148	6	145	2

Continued Table 1

Sample no.	Th	U	Pb	Th/U	Isotopic ratios						Age (Ma)					
					$^{207}Pb/^{206}Pb$		$^{207}Pb/^{235}U$		$^{206}Pb/^{238}U$		$^{207}Pb/^{206}Pb$		$^{207}Pb/^{235}U$		$^{206}Pb/^{238}U$	
	ppm	ppm	ppm		Ratio	1σ	Ratio	1σ	Ratio	1σ	Ages	1σ	Age	1σ	Age	1σ
13GW425-23	192.43	184.05	5.13	1.05	0.04964	0.00264	0.15541	0.00820	0.02270	0.00044	178	86	147	7	145	3
13GW425-24	114.13	145.73	3.90	0.78	0.04924	0.00400	0.15681	0.01266	0.02309	0.00048	159	143	148	11	147	3
13GW425-25	601.57	560.51	15.89	1.07	0.04919	0.00168	0.15452	0.00537	0.02278	0.00039	157	50	146	5	145	2
GW04209-01	45.54	56.00	1.90	0.81	0.06154	0.00406	0.17053	0.01091	0.02011	0.00030	658	112	160	9	128	2
GW04209-02	107.68	155.64	4.34	0.69	0.05143	0.00199	0.14164	0.00523	0.01999	0.00018	260	68	135	5	128	1
GW04209-03	47.75	67.82	3.63	0.70	0.20816	0.00344	0.72092	0.00938	0.02513	0.00018	2891	12	551	6	160	1
GW04209-04	246.81	214.66	10.09	1.15	0.06296	0.00417	0.17459	0.01147	0.02011	0.00016	707	145	163	10	128	1
GW04209-05	49.85	65.91	1.91	0.76	0.04993	0.00289	0.13847	0.00782	0.02012	0.00023	192	108	132	7	128	1
GW04209-06	434.82	456.77	13.27	0.95	0.05230	0.00113	0.14365	0.00277	0.01993	0.00013	299	32	136	2	127	1
GW04209-07	67.96	78.38	2.76	0.87	0.04982	0.00200	0.13779	0.00532	0.02006	0.00018	187	73	131	5	128	1
GW04209-08	91.10	139.26	3.93	0.65	0.05201	0.00184	0.14492	0.00487	0.02021	0.00017	286	62	137	4	129	1
GW04209-09	57.05	79.74	2.34	0.72	0.04851	0.00202	0.13657	0.00548	0.02042	0.00018	124	76	130	5	130	1
GW04209-10	142.79	209.43	5.74	0.68	0.05317	0.00126	0.14400	0.00310	0.01964	0.00013	336	37	137	3	125	1
GW04209-11	404.03	581.06	16.09	0.70	0.04941	0.00082	0.13668	0.00190	0.02006	0.00011	167	22	130	2	128	1
GW04209-12	55.23	74.85	2.25	0.74	0.05193	0.00198	0.14498	0.00530	0.02024	0.00018	282	67	137	5	129	1
GW04209-13	347.97	391.32	11.39	0.89	0.05324	0.00099	0.14774	0.00238	0.02012	0.00012	339	26	140	2	128	1
GW04209-14	117.18	128.78	3.73	0.91	0.05189	0.00267	0.13522	0.00686	0.01890	0.00017	280	121	129	6	121	1
GW04209-15	247.20	323.29	9.06	0.76	0.05123	0.00135	0.14311	0.00368	0.02026	0.00013	251	62	136	3	129	1
GW04209-16	321.83	352.63	10.58	0.91	0.05058	0.00104	0.14001	0.00258	0.02007	0.00013	222	31	133	2	128	1
GW04209-17	236.49	285.14	8.45	0.83	0.04980	0.00102	0.13808	0.00251	0.02010	0.00013	186	30	131	2	128	1
GW04209-18	351.12	442.39	12.15	0.79	0.04894	0.00093	0.13729	0.00229	0.02033	0.00012	145	28	131	2	130	1
GW04209-19	190.87	208.29	10.63	0.92	0.06897	0.00341	0.19187	0.00936	0.02018	0.00015	898	104	178	8	129	1
GW04209-20	400.31	414.06	12.79	0.97	0.04926	0.00090	0.14052	0.00222	0.02068	0.00012	160	26	134	2	132	1
GW04209-21	397.66	487.28	18.18	0.82	0.05600	0.00179	0.14146	0.00425	0.01831	0.00016	452	51	134	4	117	1
GW04209-22	314.92	346.15	9.88	0.91	0.04980	0.00109	0.13808	0.00273	0.02010	0.00013	186	34	131	2	128	1
GW04209-23	172.54	197.76	6.03	0.87	0.04886	0.00137	0.13812	0.00362	0.02049	0.00015	141	48	131	3	131	1

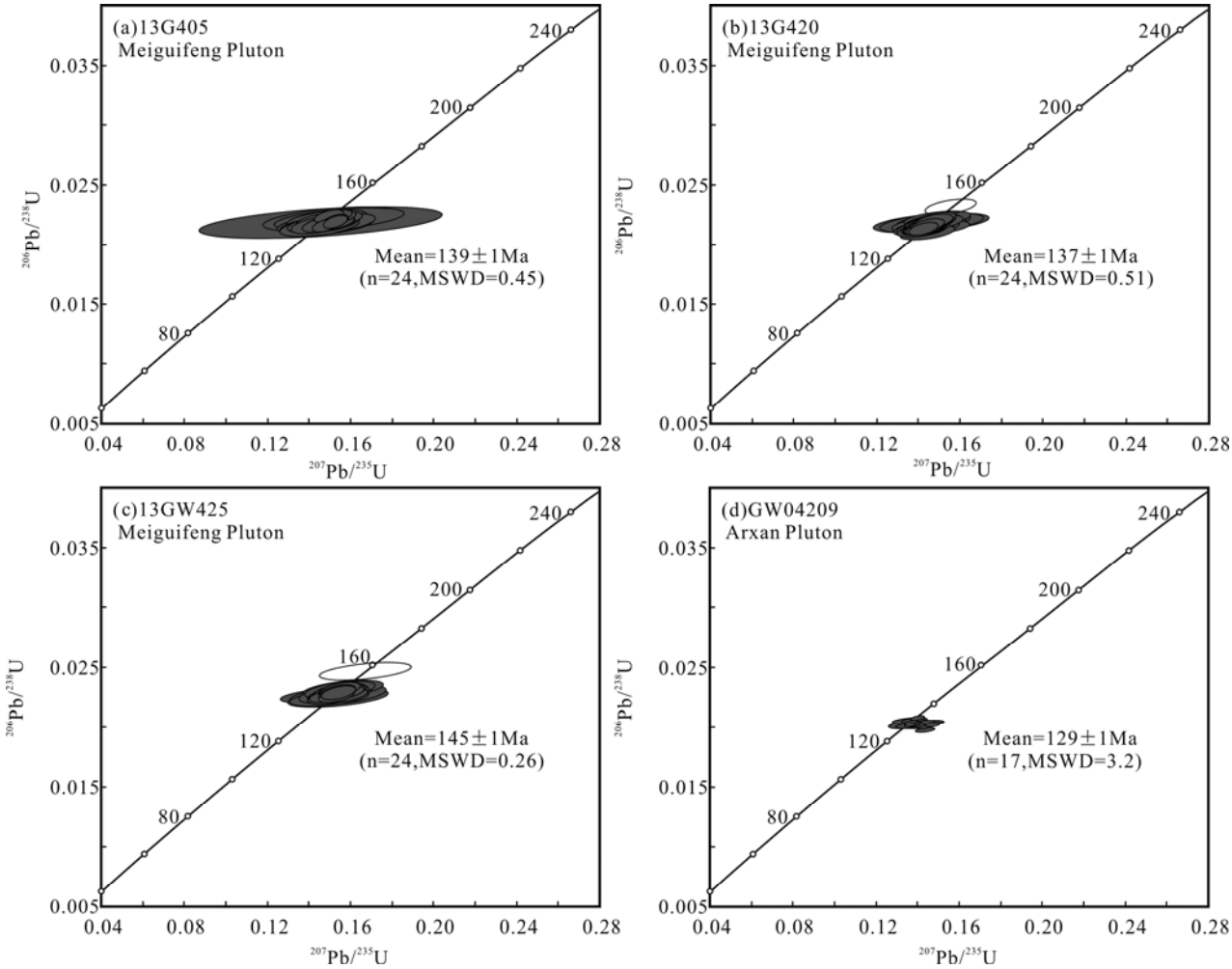

Fig. 5. Zircon LA-ICP-MS U-Pb concordia diagrams for the Meiguifeng and Arxan plutons in Great Xing'an Range. The weighted mean age and MSWD are shown in each figure.

Table 2 *In* situ zircon Hf isotopic data for the granites from Meiguifeng and Arxan plutons in Great Xing'an Range

Sample	t(Ma)	$^{176}Yb/^{177}Hf$(corr)	$^{176}Lu/^{177}Hf$(corr)	$^{176}Hf/^{177}Hf$	$2\sigma_m$	$\varepsilon_{Hf}(0)$	$\varepsilon_{Hf}(t)$	2σ	T_{DM1}	T_{DM2}	$f_{Lu/Hf}$
13GW405-01	138	0.030125	0.001143	0.282883	0.000028	3.94	6.87	0.99	524	753	−0.97
13GW405-02	142	0.035511	0.001364	0.282938	0.000032	5.88	8.87	1.14	449	628	−0.96
13GW405-03	138	0.045505	0.001720	0.282834	0.000033	2.20	5.07	1.18	604	868	−0.95
13GW405-04	141	0.038981	0.001482	0.282885	0.000035	3.98	6.94	1.23	528	751	−0.96
13GW405-05	140	0.025451	0.000996	0.282803	0.000035	1.10	4.08	1.22	636	933	−0.97
13GW405-06	136	0.041135	0.001543	0.282870	0.000034	3.48	6.33	1.21	549	786	−0.95
13GW405-07	138	0.041270	0.001556	0.282841	0.000033	2.45	5.34	1.15	591	851	−0.95
13GW405-08	138	0.030324	0.001152	0.282850	0.000034	2.76	5.68	1.21	572	829	−0.97
13GW405-09	138	0.035344	0.001318	0.282837	0.000030	2.30	5.21	1.05	593	859	−0.96
13GW405-10	137	0.020560	0.000778	0.282821	0.000032	1.74	4.68	1.12	607	893	−0.98
13GW405-11	137	0.038198	0.001494	0.282874	0.000029	3.62	6.49	1.02	542	776	−0.96
13GW405-12	138	0.044445	0.001625	0.282879	0.000032	3.80	6.68	1.13	537	765	−0.95
13GW405-13	138	0.033855	0.001279	0.282882	0.000030	3.90	6.81	1.06	528	757	−0.96
13GW405-14	137	0.035069	0.001376	0.282869	0.000036	3.43	6.31	1.28	548	788	−0.96
13GW405-15	140	0.020634	0.000800	0.282892	0.000033	4.26	7.26	1.18	507	730	−0.98
13GW405-16	138	0.031905	0.001247	0.282904	0.000035	4.69	7.60	1.23	496	706	−0.96
13GW405-17	140	0.041566	0.001556	0.282899	0.000029	4.50	7.43	1.03	508	719	−0.95
13GW405-19	141	0.029116	0.001110	0.282865	0.000031	3.29	6.28	1.11	550	793	−0.97
13GW405-20	140	0.047041	0.001788	0.282866	0.000032	3.34	6.25	1.12	558	794	−0.95
13GW420-01	139	0.033212	0.001232	0.282948	0.000033	6.21	9.15	1.18	434	607	−0.96
13GW420-02	138	0.045776	0.001639	0.282856	0.000029	2.99	5.87	1.01	570	817	−0.95
13GW420-03	135	0.042243	0.001500	0.282874	0.000030	3.62	6.46	1.07	542	777	−0.95
13GW420-04	139	0.062077	0.002202	0.282847	0.000029	2.66	5.51	1.02	593	841	−0.93
13GW420-05	139	0.041470	0.001510	0.282917	0.000030	5.12	8.03	1.05	482	679	−0.95
13GW420-06	139	0.032206	0.001210	0.282890	0.000030	4.18	7.12	1.08	516	738	−0.96
13GW420-07	139	0.027832	0.001043	0.282911	0.000033	4.92	7.88	1.15	484	689	−0.97
13GW420-08	139	0.054693	0.001930	0.282894	0.000028	4.32	7.19	0.98	520	733	−0.94
13GW420-09	139	0.039642	0.001481	0.282868	0.000033	3.39	6.30	1.18	552	790	−0.96
13GW420-10	137	0.048547	0.001755	0.282969	0.000033	6.97	9.82	1.16	409	563	−0.95
13GW420-11	138	0.039746	0.001445	0.282873	0.000028	3.59	6.49	0.99	543	778	−0.96
13GW420-12	140	0.043046	0.001590	0.282860	0.000028	3.12	6.04	1.01	564	808	−0.95
13GW420-13	136	0.040659	0.001517	0.282806	0.000031	1.19	4.04	1.10	641	933	−0.95
13GW420-14	135	0.062895	0.002249	0.282868	0.000034	3.40	6.16	1.20	563	796	−0.93
13GW420-15	136	0.040877	0.001489	0.282862	0.000030	3.19	6.04	1.04	560	805	−0.96
13GW425-01	146	0.020996	0.000823	0.282847	0.000026	2.65	5.78	0.93	571	829	−0.98
13GW425-02	146	0.043355	0.001576	0.282815	0.000029	1.52	4.58	1.03	629	906	−0.95
13GW425-04	144	0.036860	0.001364	0.282806	0.000029	1.20	4.24	1.04	638	926	−0.96
13GW425-05	144	0.041730	0.001456	0.282835	0.000031	2.24	5.27	1.09	598	860	−0.96
13GW425-06	144	0.025805	0.000957	0.282816	0.000032	1.56	4.63	1.14	617	901	−0.97
13GW425-07	143	0.028336	0.001089	0.282917	0.000034	5.12	8.15	1.19	476	675	−0.97
13GW425-08	142	0.047615	0.001747	0.282803	0.000030	1.09	4.04	1.06	650	937	−0.95
13GW425-09	144	0.028936	0.001117	0.282905	0.000032	4.71	7.77	1.15	493	700	−0.97
13GW425-10	146	0.028523	0.001124	0.282916	0.000030	5.09	8.18	1.06	478	675	−0.97
13GW425-11	144	0.044241	0.001661	0.282887	0.000032	4.07	7.08	1.12	526	744	−0.95
13GW425-12	142	0.038179	0.001414	0.282885	0.000033	3.99	6.98	1.15	526	749	−0.96
13GW425-13	144	0.031192	0.001178	0.282853	0.000036	2.87	5.92	1.26	568	819	−0.96
13GW425-14	147	0.051531	0.001862	0.282935	0.000032	5.76	8.81	1.12	460	636	−0.94
13GW425-15	144	0.024091	0.000895	0.282880	0.000029	3.84	6.91	1.02	525	755	−0.97
GW04209-02	128	0.031250	0.001021	0.282845	0.000023	2.57	5.29	0.80	578	847	−0.97
GW04209-05	128	0.027526	0.000878	0.282939	0.000026	5.89	8.63	0.91	443	633	−0.97
GW04209-06	127	0.049564	0.001693	0.282919	0.000018	5.21	7.86	0.63	480	681	−0.95
GW04209-07	128	0.022039	0.000710	0.282902	0.000020	4.59	7.34	0.69	493	715	−0.98
GW04209-08	129	0.030501	0.000992	0.282864	0.000020	3.27	6.02	0.71	549	801	−0.97
GW04209-09	130	0.039140	0.001230	0.282965	0.000020	6.82	9.57	0.71	410	574	−0.96
GW04209-10	125	0.085854	0.002550	0.282927	0.000021	5.48	8.02	0.73	481	670	−0.92
GW04209-11	128	0.059183	0.002141	0.282945	0.000021	6.11	8.74	0.74	449	626	−0.94
GW04209-12	129	0.036979	0.001220	0.282953	0.000020	6.41	9.14	0.70	426	600	−0.96
GW04209-13	128	0.036251	0.001263	0.282932	0.000021	5.65	8.36	0.75	457	650	−0.96
GW04209-15	129	0.036370	0.001203	0.282834	0.000021	2.20	4.93	0.73	596	870	−0.96
GW04209-16	128	0.054413	0.001729	0.282920	0.000025	5.23	7.89	0.88	480	680	−0.95
GW04209-17	128	0.056295	0.001856	0.282873	0.000020	3.56	6.22	0.72	550	787	−0.94
GW04209-18	130	0.022730	0.000753	0.282890	0.000019	4.17	6.95	0.66	510	742	−0.98
GW04209-20	132	0.043382	0.001222	0.282902	0.000021	4.61	7.40	0.73	498	714	−0.96
GW04209-22	128	0.033208	0.000897	0.282948	0.000019	6.21	8.95	0.66	430	612	−0.97
GW04209-23	131	0.038011	0.001156	0.282926	0.000020	5.46	8.23	0.70	464	660	−0.97

5b; MSWD=0.51, n=24). Additionally, one zircon grain yields an age of ~147 Ma. Twenty-five analytical spots for 13GW425 produce a $^{206}Pb/^{238}U$ age range 157 Ma to 142 Ma, and define a weighted mean $^{206}Pb/^{238}U$ age of 145±1 Ma (MSWD=0.26, n=24), with a single zircon age of ~157 Ma (Fig. 5c). The weighted mean $^{206}Pb/^{238}U$ age for

three Meiguifeng alkali feldspar granite samples vary from 145±1 Ma to 137±1 Ma, suggesting that they formed in the Early Cretaceous. Additionally, zircon grains from these granite samples posses relatively homogeneous Hf isotopic compositions. The $^{176}Hf/^{177}Hf$ ratios for primary zircon grains range from 0.282803 to 0.282969, and the $\varepsilon_{Hf}(t)$ values vary from +4.04 to +9.82 (Fig. 6), with two stage model ages (T_{DM2}) of 937–563 Ma.

For sample GW04209 (47°07′59.8″N, 120°03′20.5″E), a granite porphyry collected from the Arxan pluton, twenty-three zircon grains were analyzed, with six being discarded due to discordance. Seventeen analytical spots give a weighted mean $^{206}Pb/^{238}U$ age of 129±1 Ma (MSWD=3.2, n=17), representing the timing of crystallization (Fig. 5d). Primary zircons from sample GW04209 show $^{176}Hf/^{177}Hf$ ratios varying from 0.282834 to 0.282965, with $\varepsilon_{Hf}(t)$ values of +4.93 to +9.57 (Fig. 6) and T_{DM2} of 870–574 Ma.

4.2 Whole-rock geochemistry

The major and trace elemental compositions of samples from Meiguifeng and Arxan plutons are listed in Table 3.

4.2.1 Meiguifeng alkali feldspar granite

The alkali feldspar granites from Meiguifeng pluton have relatively constant major elemental compositions. They contain 75.07–77.12 wt% SiO_2, 12.21–12.86 wt% Al_2O_3, 3.77–4.04 wt% Na_2O, 4.60–4.98 wt% K_2O, with Na_2O/K_2O ratios of 0.79–0.84. These granite samples are classified as the subalkalic series in the total Na_2O+K_2O vs. SiO_2 diagram (TAS; Fig. 7a; Irvine and Baragar, 1971), and they belong to high-K calc-alkaline series in the K_2O vs. SiO_2 diagram (Fig. 7b; Peccerillo and Taylor, 1976). Additionally, they have A/CNK [molar Al_2O_3/

Table 3 Major and trace element compositions for the granites from Meiguifeng and Arxan plutons in Great Xing'an Range

Sample	13GW405	13GW406	13GW425	13GW420	13GW421	13GW422	13GW423	GW04209	GW04210	GW04211	GW04212	GW04213
Pluton	Meiguifeng Pluton							Arxan Pluton				
Major element (wt%)												
SiO_2	75.07	76.05	75.45	75.84	77.12	75.52	76.61	75.37	75.98	75.95	77.37	77.31
TiO_2	0.18	0.21	0.20	0.18	0.14	0.18	0.14	0.20	0.22	0.21	0.14	0.17
Al_2O_3	12.86	12.21	12.83	12.42	12.30	12.85	12.41	12.78	12.92	12.40	11.81	12.39
TFe_2O_3	1.10	1.18	1.22	1.16	0.93	1.10	0.99	1.23	0.46	1.55	1.29	0.42
MnO	0.03	0.03	0.05	0.03	0.01	0.02	0.01	0.01	0.01	0.03	0.01	0.01
MgO	0.25	0.26	0.23	0.29	0.11	0.23	0.16	0.09	0.25	0.12	0.06	0.10
CaO	0.39	0.39	0.44	0.44	0.22	0.43	0.34	0.28	0.08	0.16	0.09	0.07
Na_2O	3.93	3.86	4.04	3.77	3.81	3.82	3.77	4.02	4.08	3.65	3.67	4.12
K_2O	4.98	4.72	4.82	4.69	4.60	4.78	4.67	4.92	4.93	4.91	4.76	4.58
P_2O_5	0.03	0.03	0.03	0.02	0.02	0.03	0.01	0.02	0.01	0.03	0.01	0.01
L.O.I	0.85	0.72	0.66	1.12	0.72	1.01	0.85	0.61	0.58	0.69	0.45	0.49
Total	99.67	99.67	99.97	99.96	99.97	99.97	99.96	99.53	99.52	99.70	99.66	99.67
Trace element (ppm)												
Li	27.6	30.4	37.4	22.1	19.1	26.1	16.0	14.6	23.4	16.5	9.4	10.2
Be	3.10	3.43	3.88	4.70	5.15	4.04	3.82	4.03	3.34	3.59	6.89	5.65
Sc	1.98	2.27	1.16	2.04	1.89	2.08	1.72	1.88	1.53	1.69	1.71	1.37
V	7.91	7.72	7.40	6.39	4.97	6.04	3.80	5.21	2.26	5.25	4.75	2.45
Cr	0.82	0.83	1.71	2.53	2.10	1.53	2.66	0.76	0.66	0.65	1.62	3.27
Co	0.44	0.46	0.49	0.58	0.23	0.40	0.62	0.17	0.20	1.50	0.61	0.15
Ni	0.43	0.46	0.44	1.65	0.80	1.74	0.93	0.80	0.14	1.06	0.35	0.45
Cu	1.37	1.47	1.63	3.08	24.00	11.30	24.00	2.01	3.03	2.83	2.68	3.83
Zn	31.0	31.7	46.6	63.7	69.0	53.4	69.5	77.2	33.2	89.9	54.2	30.5
Ga	18.6	18.7	15.6	17.6	17.5	17.6	16.1	24.1	24.1	24.1	24.5	25.1
Rb	195	191	207	210	251	237	209	260	228	262	279	209
Sr	42.5	22.5	21.4	22.8	16.8	33.4	17.1	19.3	24.4	16.8	8.8	18.5
Y	16.2	20.0	10.1	18.4	13.8	15.2	11.5	25.4	10.4	21.5	10.5	5.5
Nb	16.3	22.1	18.3	20.6	21.3	23.0	18.5	26.4	27.1	18.0	22.2	21.9
Cs	6.31	6.25	9.12	6.62	6.00	7.02	6.30	3.00	3.70	3.08	2.46	3.35
Ba	291	150	252	138	88.9	232	102	181	203	162	58.2	148
La	35.0	40.4	16.3	48.0	43.1	33.5	33.2	61.1	16.9	61.5	23.9	10.5
Ce	62.5	71.3	26.0	69.0	55.9	49.8	44.2	104.4	21.7	101.4	41.0	18.2
Pr	6.58	7.39	3.01	7.15	5.51	4.71	4.59	10.48	1.62	10.17	3.90	1.50
Nd	21.30	23.10	9.67	21.80	15.20	13.90	13.00	35.24	4.81	33.79	12.74	4.58
Sm	3.50	3.56	1.60	3.03	1.99	1.93	1.72	5.59	0.79	5.31	2.06	0.77
Eu	0.48	0.36	0.23	0.36	0.22	0.31	0.22	0.56	0.22	0.49	0.22	0.19
Gd	2.71	3.09	1.38	2.55	1.78	1.67	1.43	5.28	0.96	4.86	1.96	0.77
Tb	0.47	0.52	0.25	0.43	0.30	0.32	0.24	0.69	0.17	0.63	0.27	0.12
Dy	2.68	2.91	1.51	2.46	1.73	1.87	1.43	3.69	1.23	3.35	1.61	0.80
Ho	0.50	0.61	0.31	0.51	0.38	0.41	0.32	0.75	0.30	0.64	0.34	0.18
Er	1.76	2.00	0.99	1.68	1.40	1.50	1.10	2.24	1.07	1.83	1.03	0.61
Tm	0.33	0.39	0.21	0.35	0.28	0.33	0.24	0.38	0.21	0.31	0.20	0.13
Yb	2.37	2.82	1.44	2.63	2.40	2.61	1.90	2.79	1.73	2.21	1.56	1.09
Lu	0.36	0.42	0.21	0.44	0.39	0.43	0.32	0.46	0.31	0.36	0.26	0.21
Ta	1.43	1.84	1.57	1.81	1.67	2.00	1.60	1.82	2.13	0.88	2.33	2.03
Pb	17.6	16.9	20.3	18.5	20.8	23.0	16.8	22.8	22.2	16.9	13.3	22.3
Th	26.1	24.4	12.8	27.2	31.7	30.8	25.6	33.6	28.3	33.5	30.9	38.8
U	3.94	4.71	3.48	8.72	6.02	8.18	3.67	6.33	6.71	4.73	5.06	4.17
Zr	100	105	101	148	138	158	121	275	264	109	150	232
Hf	4.57	4.82	4.62	6.68	6.59	7.84	5.60	8.33	7.79	4.01	7.21	9.28

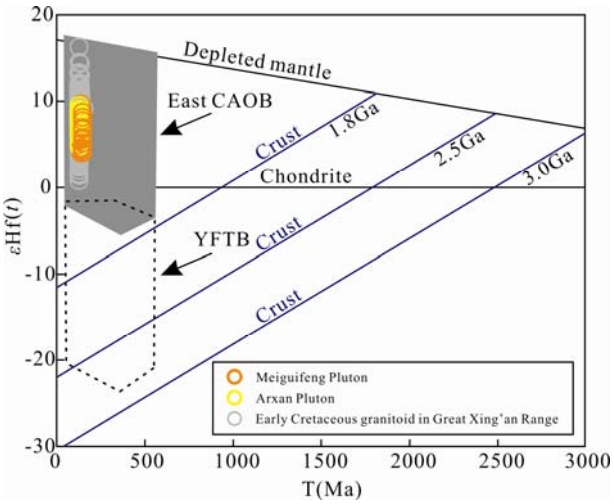

Fig. 6. The $\varepsilon_{Hf}(t)$ vs. T (Ma) diagram for the Meiguifeng and Arxan plutons in Great Xing'an Range.
Abbreviations: CAOB = Central Asian Orogenic Belt; YFTB = Yanshan Fold and Thrust Belt (Ranges of East CAOB and YFTB are from Yang et al. (2006). Granitoid data are from Zhang et al. (2008, 2018), Zhou et al. (2011), Gao et al. (2013), Shi (2015), Tian et al. (2015), Li et al. (2018a) and Xu et al. (2018).

($CaO+K_2O+Na_2O$)] values of 1.00–1.06, indicating weakly peraluminous characteristic (Fig. 7c; Maniar and Piccoli, 1989). On the chondrite-normalized rare earth element (REE) diagram (Fig. 8a), all samples have similar REE patterns, which are enriched in light rare earth elements (LREEs), with $(La/Yb)_N$ rations of 8.12–13.09. The granites also exhibit relatively significant negative Eu anomalies (Eu/Eu*=0.32–0.51). On the primitive mantle-normalized trace element spidergram (Fig. 8b), they are enriched in large ion lithophile elements (LILEs; e.g., Rb, Th, U and K), and depleted in high field strength elements (HFSEs; e.g., Nb, Ta and Ti) and P.

4.2.2 Arxan granite porphyry

The granite porphyries from Arxan pluton have similar geochemical characteristics with those from Meiguifeng pluton. These granite porphyries are high in SiO_2 (75.37–77.37 wt%) and total Na_2O+K_2O (8.43–9.01 wt%; Na_2O=3.65–4.12 wt% and K_2O=4.58–4.93 wt%), belonging to high-K calc-alkaline series (Fig. 7b; Peccerillo and Taylor, 1976). They have relatively constant A/CNK ratios (1.03–1.07), showing weakly peraluminous characteristic (Fig. 7c; Maniar and Piccoli, 1989). These granite samples also show enrichment in LREEs and LILEs (e.g., Rb, Th, U and K), and depletion in heavy rare earth elements (HREEs), HFSEs (Nb, Ta and Ti) and P (Fig. 8).

5 Discussion

5.1 Geochronology of the Early Cretaceous granitoid in NE China

Abundant granitoids are distributed in NE China, and high-precision geochronological data suggest that they are generally of Mesozoic age (Wu et al., 2002, 2011, 2015; Ge et al., 2005; Cheng et al., 2006; Zhang et al., 2008,

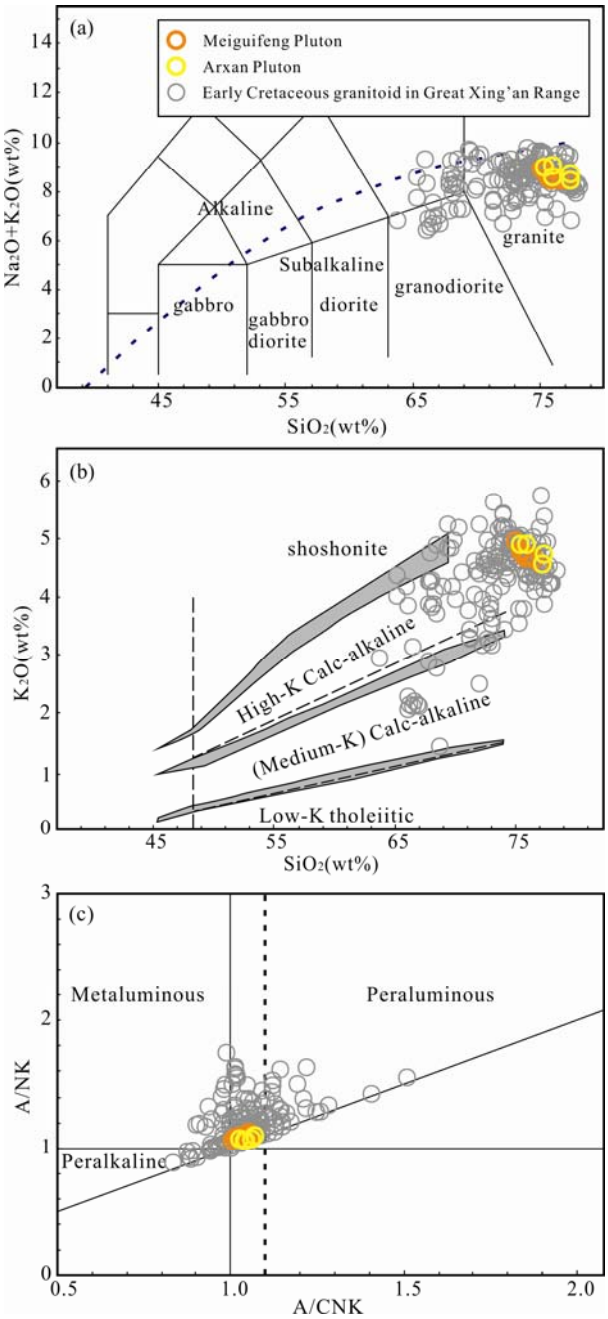

Fig. 7. Plots of (a) Na_2O+K_2O vs. SiO_2 (after Irvine and Baragar 1971), (b) K_2O vs. SiO_2 (after Peccerillo and Taylor 1976), and (c) A/NK [molar ratio Al_2O_3/(Na_2O+K_2O)] vs. A/CNK [molar ratio Al_2O_3/($CaO+Na_2O+K_2O$)] (after Maniar and Piccoli 1989), for the Meiguifeng and Arxan plutons in Great Xing'an Range.
Granitoid data are from Zhou et al. (2011), Wang et al. (2012, 2019), Gao et al. (2013), Chen et al. (2015), Shi (2015), Tian et al. (2015), Wu et al. (2015), He et al. (2017), Xie et al. (2017), Li et al. (2018a, b), Xu et al. (2018), Yin et al. (2018) and Zhang et al. (2018).

2018; Wilde et al., 2010; She et al., 2012; Wang et al., 2012b, 2019; Gao et al., 2013; Shi et al., 2013, 2015; Yu et al., 2013a, b; Li et al., 2014, 2015a, b, 2018a, b; Bi et al., 2015; Chen et al., 2015; Tian et al., 2015; Dong et al., 2016a, b; Ji et al., 2016a, b, 2018a, 2019; He et al., 2017,

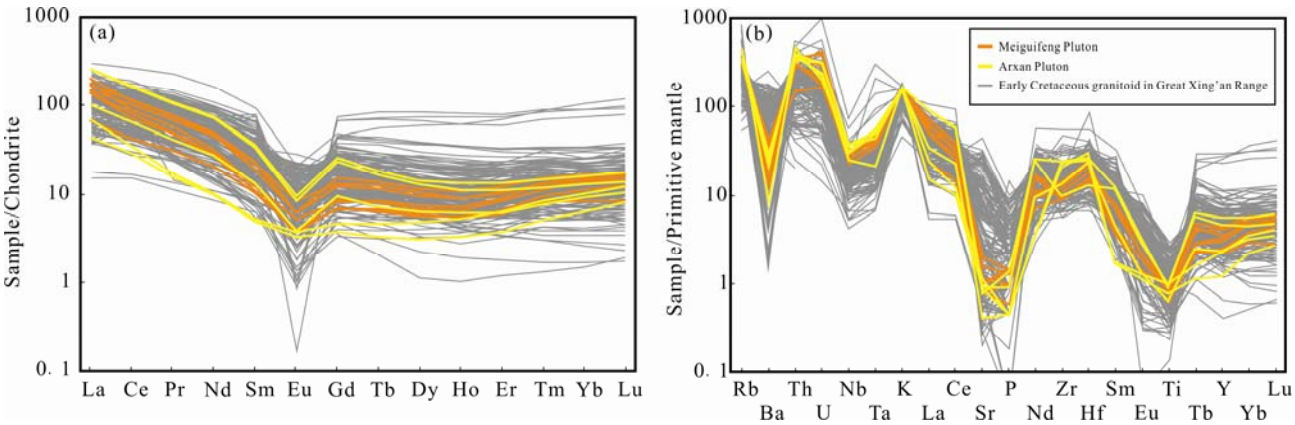

Fig. 8. Chondrite-normalized REE patterns (a) and primitive-mantle (PM)-normalized trace element) b) diagrams for the Meiguifeng and Arxan plutons in Great Xing'an Range.

Granitoid data are from Zhou et al. (2011), Wang et al. (2012, 2019), Gao et al. (2013), Chen et al. (2015), Shi (2015), Tian et al. (2015), Wu et al. (2015), He et al. (2017), Xie et al. (2017), Li et al. (2018a, b), Xu et al. (2018), Yin et al. (2018) and Zhang et al. (2018).

2018; Xie et al., 2017; Xu et al., 2018; Yin et al., 2018). Early Cretaceous granitoid was an important period of magmatism in NE China, playing a significant role in understanding the geodynamic mechanisms of Paleo-Pacific and Mongol-Okhotsk oceans (Table 4; Zhang et al., 2010a, b; Wu et al., 2011; She et al., 2012; Wang et al., 2012a, 2015; Shi et al., 2013, 2015; Xu et al., 2013a, b; Tian et al., 2015; Li et al., 2018a, b; Ji et al., 2016a; He et al., 2017, 2018; Xie et al., 2017). In this study, we undertook a combined study of zircon U-Pb-Hf isotopic and whole-rock geochemical analyses for Meiguifeng and Arxan plutons in the Great Xing'an Range. Zircon U-Pb dating by LA-ICP-MS gave emplacement ages of 145 ± 1 Ma, 139 ± 1 Ma, 137 ± 1 Ma and 129 ± 1 Ma, suggesting the Early Cretaceous magmatism occurred in the Xing'an Massif (Fig. 5). Our data, combined with zircon U-Pb ages obtained from granitoids in Erguna, Xing'an and western Songnen-Zhangguangcai Range massifs (Wu et al., 2002, 2011, 2015; Ge et al., 2005; Zhang et al., 2008, 2018; She et al., 2012; Wang et al., 2012b, 2019; Gao et al., 2013; Shi et al., 2013, 2015; Chen et al., 2015; Li et al., 2018a, b; Tian et al., 2015; Ji et al., 2016a; He et al., 2017, 2018; Xie et al., 2017; Xu et al., 2018; Yin et al., 2018), indicate the extensive Early Cretaceous magmatism in Great Xing'an Range. However, the Lesser Xing'an Range is characterized by Jurassic magmatism instead of Early Cretaceous magmatic activity (Wu et al., 2000, 2002, 2011; Sun et al., 2005), and the Early Cretaceous granitoids are not widely distributed in Jiamusi Massif and Nadanhada Terrane (Cheng et al., 2006; Wilde et al., 2010; Bi et al., 2015; Dong et al., 2016a). The temporal-spatial distribution of Early Cretaceous granitoid in NE China provides important information in deciphering both magmatism and tectonic evolution of CAOB.

5.2 Petrogenesis

5.2.1 Granite type

Commonly, granites can be divided into I-, S-, M- and A-types, which are known to provide important information on the origin and nature of magma, as well as the tectonic evolution history (Pitcher, 1982; Eby, 1990; Chappell and White, 1974, 1992, 2001). The I- and S-type granite subdivision was firstly proposed by Chappell and White (1974), and their magmas were derived from partial melting of metaigneous rocks and metasedimentary rocks, respectively. These two type granites come from distinct source materials, exhibiting different petrological and geochemical features. In general, I-type granites are metaluminous to weakly peraluminous (A/CNK ratios<1.1), whereas S-type granites are peraluminous in compositions with A/CNK ratios> 1.1. S-type granites usually contain Al-rich minerals (e.g., muscovite and cordierite), while hornblende is common in I-type granites. Moreover, the liner correlation in oxidation can give rise to useful field criteria for distinguishing I- and S-type granites (Chappell and White, 2001). The negative correlation between P_2O_5 and SiO_2 is indicative of I-type granite trend, and the positive correlation shows S-type granite trend. It is because that phosphorus commonly reaches saturation in metaluminous and weakly peraluminous magmas, however, it highly dissolves in peraluminous melts (Wolf and London, 1994). The liner correlation in Th vs. Rb is also a crucial criterion for distinguishing granite types. The Th-enriched minerals separate from peraluminous magmas in the early stage, but they are compatible in metaluminous melts. Therefore, Th concentrations are relatively low in S-type granites but high in I-type granites. As for M-type granite, its formation is generally related to differentiation of mantle-derived basic magma, showing mantle-derived characteristics. In addition, A-type granite was initially defined as the anhydrous and low oxygen fugacity granite derived from alkali basic magma (Loiselle and Wones, 1979). During the past decades, the definition has broadened, attracting much more attention (Loiselle and Wones, 1979; Collins et al., 1982; Whalen et al., 1987; Eby, 1990, 1992; Bonin 2007; Jiang et al., 2017). A-type granites contain annite-rich biotite and/or alkali hornblende and commonly sodic pyroxene (Whalen *et al.* 1987), with high zircon saturation temperatures (>850°C). Geochemically, A-type granite is characterized by high SiO_2, total alkali, Zr, Nb, Ga, Sn, Y, F and REE (except

Table 4 Geochronological data for the Early Cretaceous granitic rocks in NE China

Order	Sample	GPS location	Pluton	Lithology	Method	Age	References
Erguna Massif							
1	0066-5	N50°40′00″, E121°36′00″	Yitulihe	Granodiorite	LA-ICP-MS	118 ± 1 Ma	Wu et al. (2011)
2	0116-1	N51°26′18″, E122°14′40″	Niuerhe	Alkali feldspar granite	LA-ICP-MS	125 ± 2 Ma	Wu et al. (2011)
3	SPM3TC27	N51°48′35″, E121°53′24″	Tahe	Monzogranite	LA-ICP-MS	127 ± 1 Ma	Xu et al. (2018)
4	JGD-33	N51°17′35″, E124°14′02″	Xintianzhenbei	Granite	LA-ICP-MS	128 ± 1 Ma	She et al. (2012)
5	JGD-34	N51°15′42″, E124°11′57″	Xintianzhenbei	Syenogranite	LA-ICP-MS	128 ± 1 Ma	She et al. (2012)
6	0076-9	N51°37′40.1″, E124°09′22.9″	Qianjinlinchang	Granodiorite	LA-ICP-MS	131 ± 3 Ma	Zhang et al. (2008)
7	0075-7	N51°36′22.7″, E124°19′26.2″	Linhai	Granodiorite	LA-ICP-MS	132 ± 3 Ma	Zhang et al. (2008)
8	PM022LT58			Alkali feldspar granite	LA-ICP-MS	138 ± 1 Ma	Yin et al. (2018)
9	D0410			Alkali feldspar granite	LA-ICP-MS	140 ± 1 Ma	Yin et al. (2018)
10	WLS-16	N49°26′21.4″, E117°06′03.5″	Wunugetushan	Granite	LA-ICP-MS	144 ± 3 Ma	She et al. (2012)
Xing'an Massif							
1	9832-2	N50°21′30″, E127°18′15″	Shangmachang	Syenogranite	TIMS	106 ± 2 Ma	Wu et al. (2002)
2	GW04364	N46°54′42.8″, E122°08′29.4″	Shenshan	Alkali feldspar granite	LA-ICP-MS	120 ± 1 Ma	Chen et al. (2015)
3	GW04459	N50°35′26″, E124°16′36″	Cuifeng	Plagiogranite	LA-ICP-MS	122 ± 1 Ma	Wu et al. (2011)
4	GW04448	N50°47′58″, E124°07′33″	Yaolinger	Syenogranite	LA-ICP-MS	125 ± 1 Ma	Wu et al. (2011)
5	Z11-62	N47°04′33″, E120°50′17″	Hamagou	Monzonitic porphyry	LA-ICP-MS	126 ± 1 Ma	Shi et al. (2013)
6	D0627-2-1	N46°51′08″, E120°43′27″	Wuchagou	Syenogranite	LA-ICP-MS	127 ± 1 Ma	Xie et al. (2017)
7	MP22-6	N46°35′01″, E121°14′01″	Suolunzhen	Syenogranite	LA-ICP-MS	128 ± 1 Ma	Wang et al. (2019)
8	GW04278	N47°53′11″, E122°02′24″	Bijiadian	Syenite porphyry	LA-ICP-MS	128 ± 1 Ma	Chen et al. (2015)
9	JGD-35	N50°25′57″, E124°05′17″	Jiagedaqi	Monzogranite	LA-ICP-MS	128 ± 1 Ma	She et al. (2012)
10	YL1	N47°25′00″, E124°18′00″	Yili deposit	Granite porphyry	SHRIMP	128 ± 2 Ma	Wu et al. (2015)
11	D2612-3-1	N46°42′11″, E120°30′41″	Wuchagou	Granite porphyry	LA-ICP-MS	129 ± 1 Ma	Xie et al. (2017)
12	Z10-32	N47°57′50″, E121°54′48″	Jiqinhe	Monzogranite	LA-ICP-MS	129 ± 1 Ma	Shi et al. (2015)
13	Z10-39	N47°41′18″, E122°29′12″	Zhonghe	Granite porphyry	LA-ICP-MS	129 ± 1 Ma	Shi et al. (2015)
14	BKT-11	N47°54′53.7″, E122°44′33.4″	Boketu-Zhalantun	Syenite porphyry	LA-ICP-MS	129 ± 1 Ma	She et al. (2012)
15	TED-32	N48°29′25″, E121°20′53″	Chuoer-Wunuer	Plagiogranite	LA-ICP-MS	129 ± 1 Ma	She et al. (2012)
16	GW04209	N47°07′59.8″, E120°03′20.5″	Arxan	Granite porphyry	LA-ICP-MS	129 ± 1 Ma	This study
17	FW04-403	N49°33′41″, E123°45′44″	Longtou	Monzogranite	LA-ICP-MS	129 ± 2 Ma	Wu et al. (2011)
18	GW04278	N47°53′11″, E122°02′24″	Jiqinhe	Quartz syenite	LA-ICP-MS	129 ± 2 Ma	Wu et al. (2011)
19	PM014-8-1	N46°46′40″, E120°42′37″	Wuchagou	Monzogranite	LA-ICP-MS	129 ± 2 Ma	Xie et al. (2017)
20	YL3	N47°25′00″, E124°18′00″	Yili deposit	Granite porphyry	SHRIMP	129 ± 4 Ma	Wu et al. (2015)
21	FW04-413	N49°10′38″, E123°45′33″	Nuomin	Monzogranite	LA-ICP-MS	130 ± 1 Ma	Wu et al. (2011)
22	FW04-407	N49°14′31″, E123°46′04″	Yilinongchang	Monzogranite	LA-ICP-MS	131 ± 1 Ma	Wu et al. (2011)
23	GW04271	N47°52′36″, E121°20′27″	Bashenghe	Syenogranite	LA-ICP-MS	131 ± 1 Ma	Wu et al. (2011)
24	Z10-37	N47°46′25″, E122°36′50″	Zhonghe	Monzogranite	LA-ICP-MS	131 ± 1 Ma	Shi et al. (2015)
25	BKT-05	N48°34′51.9″, E122°07′07.7″	Boketu-Zhalantun	Granite	LA-ICP-MS	131 ± 1 Ma	She et al. (2012)
26	TS-55	N50°14′53.4″, E125°47′34.5″	Tongshan	Granite	LA-ICP-MS	131 ± 1 Ma	She et al. (2012)
27	D0299-1-1	N46°56′27″, E120°38′44″	Wuchagou	Granite porphyry	LA-ICP-MS	131 ± 2 Ma	Xie et al. (2017)
28	DHS-4	N50°31′58″, E124°28′34″	Songling	Porphyritic granite	LA-ICP-MS	131 ± 3 Ma	Zhang et al. (2018)
29	16DX5-1	N47°42′24″, E122°35′49″	Zhalantun	Syenogranite	LA-ICP-MS	132 ± 1 Ma	Li et al. (2018a)
30	PM014-3-1	N46°46′11″, E120°43′01″	Wuchagou	Granite porphyry	LA-ICP-MS	132 ± 1 Ma	Xie et al. (2017)
31	13GW262	N48°31′52″, E121°48′06″	Ailinyuan	Monzogranite	LA-ICP-MS	132 ± 2 Ma	He et al. (2017)
32	DHS-2	N50°32′21″, E124°26′53″	Songling	Porphyritic granite	LA-ICP-MS	132 ± 3 Ma	Zhang et al. (2018)
33	GW04309	N47°45′50″, E122°16′16″	Xinlitun	Monzogranite	LA-ICP-MS	133 ± 1 Ma	Wu et al. (2011)
34	D2615	N46°42′04″, E120°22′36″	Wuchagou	Syenogranite	LA-ICP-MS	133 ± 1 Ma	Xie et al. (2017)
35	Z10-26	N47°30′00″, E122°18′00″	Moguqi	Monzogranite	LA-ICP-MS	133 ± 1 Ma	Shi et al. (2015)
36	DHS-1	N50°32′11″, E124°27′13″	Songling	Porphyritic granite	LA-ICP-MS	133 ± 3 Ma	Zhang et al. (2018)
37	P30b6-3	N47°35′00″, E121°12′00″	Chaihe	Alkali feldspar granite	LA-ICP-MS	133 ± 3 Ma	Wang et al. (2012)
38	MP15-9	N46°40′39″, E121°11′20″	Suolunmachang	Syenogranite	LA-ICP-MS	134 ± 1 Ma	Wang et al. (2019)
39	D3023-1	N46°53′50″, E120°22′36″	Wuchagou	Monzogranite	LA-ICP-MS	134 ± 1 Ma	Xie et al. (2017)
40	16DX3-1	N46°19′57″, E120°41′35″	Suolun	Syenogranite	LA-ICP-MS	135 ± 1 Ma	Li et al. (2018a)
41	MP12-5	N46°42′36″, E120°51′41″	Mingshuihelinchang	Alkali feldspar granite	LA-ICP-MS	136 ± 1 Ma	Wang et al. (2019)
42	Z10-17	N47°23′09″, E121°12′20″	Hamagou	Monzogranite	LA-ICP-MS	136 ± 1 Ma	Shi et al. (2013)
43	Z11-63	N47°04′06″, E120°34′17″	Hamagou	Granite porphyry	LA-ICP-MS	136 ± 1 Ma	Shi et al. (2013)
44	GW04271	N47°52′36″, E121°20′27″	Bijiadian	Syenogranite	LA-ICP-MS	136 ± 3 Ma	Chen et al. (2015)
45	Z10-16	N47°09′22″, E121°04′45″	Hamagou	Syenogranite	LA-ICP-MS	137 ± 1 Ma	Shi et al. (2013)
46	13GW258	N48°26′30″, E121°53′41″	Ailinyuan	Monzogranite	LA-ICP-MS	137 ± 1 Ma	He et al. (2017)
47	JGD-05	N50°33′53″, E125°41′47″	Woduhe	Granite	LA-ICP-MS	137 ± 1 Ma	She et al. (2012)
48	13GW420	N47°19′31.6″, E119°41′46.4″	Meiguifeng	Alkali feldspar granite	LA-ICP-MS	137 ± 1 Ma	This study
49	YE-1	N47°16′30″, E119°47′00″	Yiershi	Syenogranite	SHRIMP	137 ± 2 Ma	Wu et al. (2011)
50	FW04-405	N49°33′03″, E123°21′29″	Dalaibin	Monzogranite	LA-ICP-MS	139 ± 1 Ma	Wu et al. (2011)
51	13GW405	N47°19′28.8″, E119°41′25.6″	Meiguifeng	Alkali feldspar granite	LA-ICP-MS	139 ± 1 Ma	This study
52	GW04276	N48°05′19″, E121°50′21″	Bijiadian	Syenogranite	LA-ICP-MS	140 ± 1 Ma	Chen et al. (2015)
53	BKT-06	N48°20′30.3″, E122°17′53.6″	Boketu-Zhalantun	Granite porphyry	LA-ICP-MS	141 ± 1 Ma	She et al. (2012)
54	13GW375	N47°43′26″, E120°29′56″	Sangduoer	Monzogranite	LA-ICP-MS	141 ± 2 Ma	Ji et al. (2016)
55	GS3460	N47°39′59″, E119°45′35″	Wuertu	Syenogranite	LA-ICP-MS	142 ± 1 Ma	Li et al. (2018b)
56	GS1201	N47°20′20″, E119°45′43″	Tuoliela	Syenogranite	LA-ICP-MS	142 ± 1 Ma	Li et al. (2018b)
57	FW04-412	N49°35′35″, E124°04′18″	Yili	Granodiorite	LA-ICP-MS	142 ± 1 Ma	Wu et al. (2011)
58	13GW308	N49°28′37″, E121°43′15″	Banlashan	Alkali feldspar granite	LA-ICP-MS	142 ± 1 Ma	He et al. (2018)
59	GW04014	N48°19′50″, E122°19′12″	Lamashan	Monzogranite	LA-ICP-MS	142 ± 3 Ma	Wu et al. (2011)
60	13GW349	N48°02′47″, E121°38′53″	Sandaoqiao	Syenogranite	LA-ICP-MS	143 ± 1 Ma	Ji et al. (2016)
61	GW04276	N48°05′19″, E121°50′21″	Sanqilinshang	Quartz syenite	LA-ICP-MS	143 ± 3 Ma	Wu et al. (2011)

Continued Table 4

Order	Sample	GPS location	Pluton	Lithology	Method	Age	References
62	13GW305	N49°28′52″, E121°40′35″	Banlashan	Monzogranite	LA-ICP-MS	144 ± 2 Ma	He et al. (2018)
63	14GW511	N49°27′20″, E121°46′14″	Banlashan	Syenogranite	LA-ICP-MS	145 ± 1 Ma	He et al. (2018)
64	TED-30	N48°27′28″, E121°12′46″	Chuoer-Wunuer	Granite	LA-ICP-MS	145 ± 1 Ma	She et al. (2012)
65	13GW425	N47°19′28.8″, E119°41′20.1″	Meiguifeng	Alkali feldspar granite	LA-ICP-MS	145 ± 1 Ma	This study
66	GW04015	N48°36′48″, E122°05′42″	Yalu	Monzogranite	LA-ICP-MS	145 ± 5 Ma	Wu et al. (2011)
Songnen-Zhangguangcai Range Massif							
1	GW04364	N46°54′43″, E122°08′29″	Shenshan	Alkali feldspar granite	LA-ICP-MS	119 ± 1 Ma	Wu et al. (2011)
2	GW04360	N46°48′21″, E122°33′00″	Caishichangxi	Monzogranite	LA-ICP-MS	120 ± 1 Ma	Wu et al. (2011)
3	GW04314	N47°22′25″, E122°12′34″	Fengshou	Syenogranite	LA-ICP-MS	120 ± 2 Ma	Wu et al. (2011)
4	Z10-03	N47°10′28″, E122°10′54″	Luotuobozi	Granodiorite	LA-ICP-MS	126 ± 1 Ma	Gao et al. (2013)
5	G0215-4	N46°36′07″, E121°15′23″	Suolun	Alkali feldspar granite	LA-ICP-MS	126 ± 2 Ma	Ge et al. (2005)
6	Z10-02	N47°10′35″, E122°12′43″	Luotuobozi	Syenogranite	LA-ICP-MS	127 ± 1 Ma	Gao et al. (2013)
7	G0206-1	N46°29′24″, E122°29′13″	Yonghetun	Monzogranite	LA-ICP-MS	127 ± 2 Ma	Ge et al. (2005)
8	G0206-2	N46°29′24″, E122°29′13″	Yonghetun	Prophyrite	LA-ICP-MS	128 ± 3 Ma	Ge et al. (2005)
9	GW04162	N46°21′14″, E121°05′32″	Shabutai	Monzogranite	LA-ICP-MS	129 ± 2 Ma	Wu et al. (2011)
10	Z10-05	N47°05′40″, E122°03′00″	Luotuobozi	Monzogranite	LA-ICP-MS	130 ± 1 Ma	Gao et al. (2013)
11	GW04158	N46°24′42″, E121°14′23″	Wulanmaodu	Syenogranite	LA-ICP-MS	131 ± 1 Ma	Wu et al. (2011)
12	05FW083	N43°15′08″, E117°49′12″	Baiyinbangou	Monzogranite	LA-ICP-MS	131 ± 2 Ma	Wu et al. (2011)
13	05FW116	N43°26′13″, E117°29′47″	Huanggangliang	Syenogranite	LA-ICP-MS	132 ± 1 Ma	Wu et al. (2011)
14	05FW120	N43°21′43″, E117°36′34″	Dayingzi	Monzogranite	LA-ICP-MS	132 ± 1 Ma	Wu et al. (2011)
15	05FW141	N44°09′55″, E118°16′28″	Chaoyanggou	Monzogranite	LA-ICP-MS	132 ± 1 Ma	Wu et al. (2011)
16	Z11-60	N47°07′13″, E122°04′20″	Luotuobozi	Granite porphyry	LA-ICP-MS	132 ± 2 Ma	Shi et al. (2015)
17	G0208-3	N46°29′41″, E122°07′29″	Qingshan	Monzogranite	LA-ICP-MS	133 ± 3 Ma	Ge et al. (2005)
18	12GW104	N46°42′10″, E120°50′52″	Mingshui	Alkali feldspar granite	SIMS	134 ± 1 Ma	Tian et al. (2015)
19	12GW105	N46°42′11″, E120°50′36″	Mingshui	Alkali feldspar granite	SIMS	134 ± 1 Ma	Tian et al. (2015)
20	GW04369	N46°40′58″, E121°13′11″	Suolunjunmachang	Alkali feldspar granite	SIMS	134 ± 1 Ma	Tian et al. (2015)
21	05FW066	N43°14′02″, E117°31′54″	Jingpeng	Quartz syenite	LA-ICP-MS	134 ± 1 Ma	Wu et al. (2011)
22	GW04369	N46°40′58″, E121°13′11″	Suolun	Alkali feldspar granite	LA-ICP-MS	134 ± 2 Ma	Wu et al. (2011)
23	GW04190	N46°36′30″, E120°53′55″	Jilasitai	Alkali feldspar granite	LA-ICP-MS	135 ± 2 Ma	Wu et al. (2011)
24	GW04190	N46°36′30″, E120°53′55″	Jilasitainangou	Alkali feldspar granite	SIMS	136 ± 1 Ma	Tian et al. (2015)
25	05FW171	N43°57′15″, E117°32′24″	Beidashan	Syenogranite	LA-ICP-MS	136 ± 2 Ma	Wu et al. (2011)
26	G0208-1	N46°29′41″, E122°07′29″	Qingshan	Monzogranite	LA-ICP-MS	138 ± 3 Ma	Ge et al. (2005)
27	05FW163	N44°04′54″, E117°43′05″	Beidashan	Granodiorite	LA-ICP-MS	139 ± 1 Ma	Wu et al. (2011)
28	05FW065	N43°13′33″, E117°32′30″	Jingpeng	Monzogranite	LA-ICP-MS	140 ± 2 Ma	Wu et al. (2011)
29	05FW080	N43°15′50″, E117°44′55″	Jingpeng	Monzogranite	LA-ICP-MS	140 ± 2 Ma	Wu et al. (2011)
30	05FW064	N43°13′33″, E117°32′30″	Jingpeng	Monzogranite	LA-ICP-MS	141 ± 1 Ma	Wu et al. (2011)
31	05FW124	N43°31′09″, E117°37′27″	Huanggangliang	Syenogranite	LA-ICP-MS	141 ± 1 Ma	Wu et al. (2011)
32	05FW147	N44°07′36″, E118°10′03″	Chaoyanggou	Monzogranite	LA-ICP-MS	142 ± 3 Ma	Wu et al. (2011)
33	05FW121	N43°29′56″, E117°39′05″	Huanggangliang	Monzogranite	LA-ICP-MS	146 ± 2 Ma	Wu et al. (2011)
Jiamusi Massif							
1	13GW043	N46°12′15″, E132°59′27″	Shuguang	Granite porphyry	LA-ICP-MS	110 ± 1 Ma	Bi et al. (2015)
2	18YL024		Jinbu	Granodiorite	LA-ICP-MS	111 ± 1 Ma	Unpublished data
3	13GW130		Zhouyutang	Granite	LA-ICP-MS	112 ± 2 Ma	Unpublished data
4	14GW058		Hongtai	Granite porphyry	LA-ICP-MS	120 ± 1 Ma	Unpublished data
5	15GW240	N46°05′57″, E130°41′09″	Huanan	Granite porphyry	LA-ICP-MS	123 ± 1 Ma	Dong et al. (2016)
Nadanhada Terrane							
1	FW04-251	N46°54′43″, E133°44′25″	Mayihe	Granodiorite	LA-ICP-MS	124 ± 1 Ma	Cheng et al. (2006)
2	FW04-239	N46°48′52″, E133°50′49″	Mayihe	Granodiorite	LA-ICP-MS	124 ± 1 Ma	Cheng et al. (2006)
3	FW04-257	N47°04′36″, E133°53′47″	Mayihe	Granodiorite	LA-ICP-MS	116 ± 1 Ma	Cheng et al. (2006)
4	FW04-246	N46°43′31″, E133°52′49″	Taipingcun	Syenogranite	LA-ICP-MS	114 ± 1 Ma	Cheng et al. (2006)
5	FW04-254	N47°04′36″, E133°53′47″	Mayihe	Granodiorite	LA-ICP-MS	114 ± 1 Ma	Cheng et al. (2006)
6	FW04-272	N45°48′00″, E132°55′16″	Hulin	Granodiorite	LA-ICP-MS	112 ± 1 Ma	Wilde et al. (2010)
7	FW04-244	N46°46′32″, E133°49′27″	Taipingcun	Syenogranite	LA-ICP-MS	111 ± 1 Ma	Cheng et al. (2006)

Eu) concentrations, but low CaO, Al_2O_3, Sr and Ba contents, with high Fe/Mg and Ga/Al ratios (Loiselle and Wones, 1979; Collins et al., 1982; Whalen et al., 1987; Eby, 1990, 1992; Bonin, 2007; Jiang et al., 2017).

For the granite porphyries from Arxan pluton in this study, it is easy to preclude the possibility of S- and M-type granites. These granite porphyries are high in SiO_2 (75.37–77.37 wt%) and differentiation index (96.3–98.3), making difficulties in distinguishing the granite type. Because the highly evolved granites would show mineralogical and geochemical characteristics comparable to the haplogranite (near minimum-temperature melt), the petrogenetic schemes related to discrimination between A-type granites and highly fractionated I-type granites could be complicated (King et al., 1997). Moreover, their 10000*Ga/Al ratios (3.53–3.91) are greater than 2.6, but we can't attribute them to A-type granites based simply on high Ga/Al ratios. Generally, the generation of typical A-type granites is under high temperature conditions, however, these granite porphyries have relatively low zircon saturation temperatures (762–839 °C), which is similar to I-type granites. Furthermore, they mostly fall in the field of highly fractionated area in $(Al_2O_3+CaO)/(TFe_2O_3+Na_2O+K_2O)$ vs. $100*(MgO+TFe_2O_3+TiO_2)/SiO_2$ and 10000×Ga/Al vs. Zr+Nb+Ce+Y diagrams (Figs. 9c and 9d). Combined with above geochemical

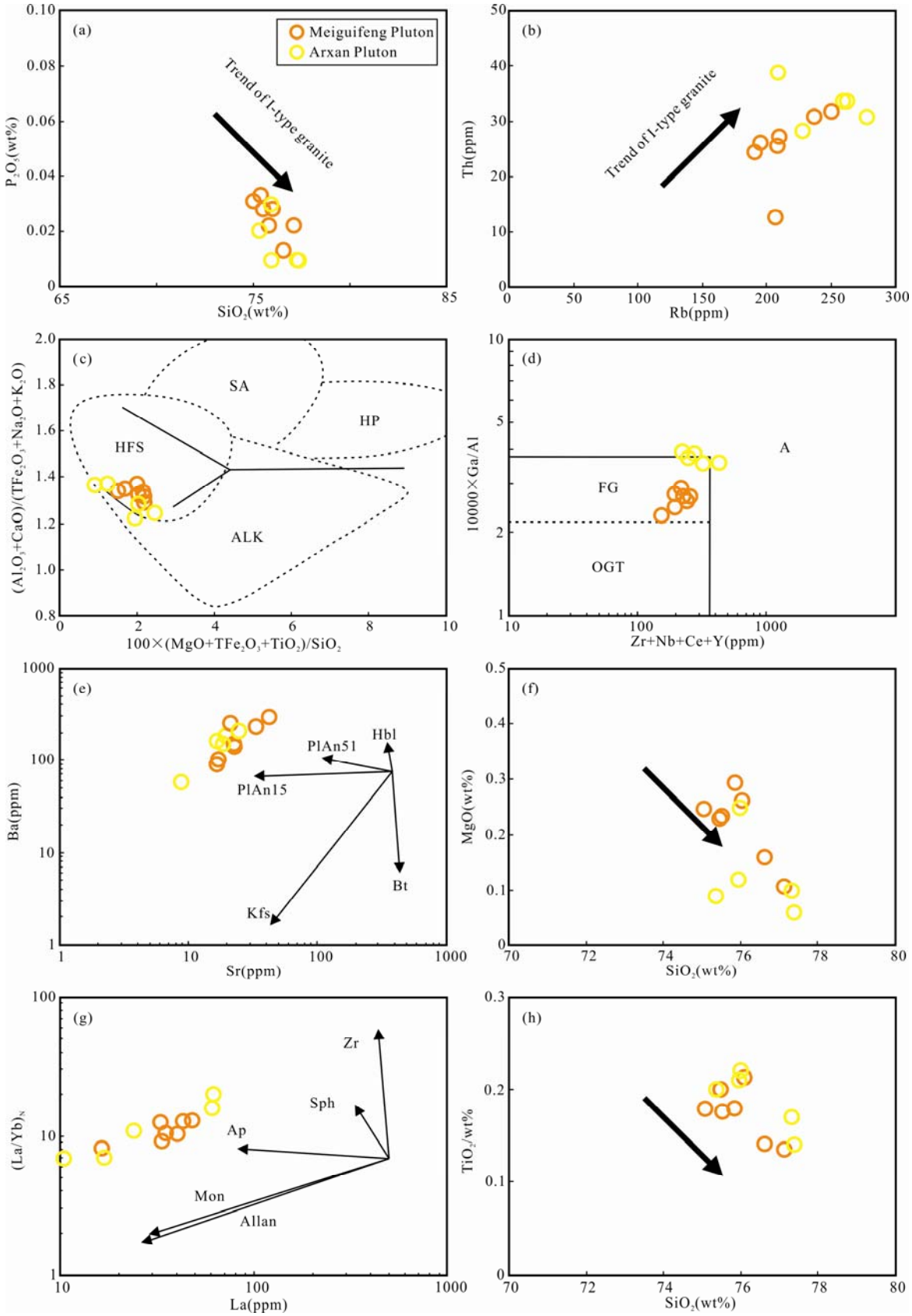

Fig. 9. Plots of (a) P_2O_5 vs. SiO_2; (b) Th vs. Rb; (c) $(Al_2O_3+CaO)/(TFe_2O_3+Na_2O+K_2O)$ vs. $100*(MgO+TFe_2O_3+TiO_2)/SiO_2$; (d) 10000×Ga/Al vs. Zr+Nb+Ce+Y; (e) Ba vs. Sr; (f) MgO vs. SiO_2; (g) (La/Yb)N vs. La; (h) TiO_2 vs. SiO_2.
Abbreviations: SA = subalkaline type; HFS = highly fractionated subalkaline type; HP = highly peraluminous type; ALK = alkaline type; FG = highly fractionated I-type; OGT = unfractionated I, S and M type; A = A type; Pl = plagioclase; Kfs = K-feldspar; Bt = biotite; Hbl = hornblende; Zr = zircon; Sph = titanite; Ap = apatite; Mon = monazite; Allan = allanite.

characteristics, we suggest that the granite porphyries from Arxan pluton are highly fractionated I-type granites. With respect to the alkali feldspar granites from Meiguifeng pluton, they also have high SiO_2 contents (75.07–77.12 wt%), with high differentiation index (95.4–96.9). These alkali feldspar granites show weakly peraluminous feature (A/CNK =1.00–1.06), and their P_2O_5 concentrations decrease with increasing SiO_2 (Fig. 9a), suggesting typical I-type granite affinity. Moreover, their Th contents increase with increasing Rb concentrations (Fig. 9b). The alkali feldspar granite samples mostly plot in the field of highly fractionated area in the discrimination diagrams (Figs. 9a and 9b), further confirming their highly fractionated I-type granite affinity.

5.2.2 Fractional crystallization

The fractional crystallization can play a crucial role in the magma evolution. The Meiguifeng and Arxan plutons are highly fractionated I-type granites, and they are characterized by high silica, total alkalis, differentiation index and low Cao, MgO, TFe_2O_3 concentrates, with remarkable negative Ba, Sr, Eu, P, Nb, Ta and Ti anomalies (Fig. 8b), suggesting they underwent a fractional crystallization process in the magma evolution. Along with the formation of Meiguifeng and Arxan plutons, the fractionation of plagioclase and K-feldspar has been taking place, as evidenced by the depletion in Ba, Sr and Eu (Fig. 8; Harris et al., 1990). Moreover, the variation trend in Ba vs. Sr, K_2O vs. SiO_2 and MgO vs. SiO_2 diagram indicate the fractionation of plagioclase, K-feldspar and biotite (Figs. 9e and 9f). Low P_2O_5 contents (0.01–0.03 wt%) and negative P anomalies are considered to be associated with the apatite fractionation (Fig. 8b). The variation trends in $(La/Yb)_N$ vs. La also argue monazite and allanite as fractionation minerals (Fig. 9g), suggesting that monazite and allanite played dominant roles in controlling REE concentrations. The negative linear correlations in TiO_2 vs. SiO_2 and negative Nb, Ta and Ti anomalies (Figs. 8b and 9h) show the fractionation of Ti-bearing phases (e.g., rutile, titanite and ilmenite). Taken together, plagioclase, K-feldspar, biotite, apatite, monazite, allanite and Ti-bearing phases fractionated from the magma during the generation of Meiguifeng and Arxan plutons.

5.2.3 Magma source

In general, highly fractionated I-type granites have been proposed to be formed by two different petrogenetic models, including (1) partial melting of the lower crust with compositions then may have experienced extensive fractional crystallization (Miller, 1985; Barbarin, 1996; Chappell et al., 2012) and (2) high degree of crystal fractionation for clinopyroxene and hornblende from intermediate to basic melts (Cawthorn and Brown, 1976; Wyborn et al., 1987, 2001).

It is noteworthy that NE China is characterized by large volumes of granitoids, and Early Cretaceous granitoids play an important part in the magmatism of continental margin of northeastern Asia (Wu et al., 2002, 2011, 2015; Ge et al., 2005; Cheng et al., 2006; Zhang et al., 2008, 2018; Wilde et al., 2010; She et al., 2012; Wang et al., 2012b, 2019; Gao et al., 2013; Shi et al., 2013, 2015; Yu et al., 2013a, b; Li et al., 2014, 2015a, b, 2018a, b; Bi et al., 2015; Chen et al., 2015; Tian et al., 2015; Dong et al., 2016a, b; Ji et al., 2016a, b, 2018a, 2019; He et al., 2017, 2018; Xie et al., 2017; Xu et al., 2018; Yin et al., 2018). Meanwhile, the study area is composed mainly of Mesozoic granitoids and volcanic rocks, with some Cenozoic basalts (Fig. 2). These Mesozoic volcanic rocks are mainly acidic volcanic rocks, with minor intermediate volcanics, and they were mainly generated by partial melting of lower crustal materials (Zhang, 2006, 2009; Zhang et al., 2010a; Dong et al., 2014; Ji et al., 2016b). Together, it is difficult to explain the formation of Early Cretaceous Meiguifeng and Arxan plutons in the Great Xing'an Range through the second model. Both Meiguifeng and Arxan plutons contain high SiO_2 contents (75.07–77.12 wt% and 75.37–77.37 wt%), with low MgO (0.11–0.29 wt% and 0.06–0.25 wt%), TFe_2O_3 (0.93–1.22 wt% and 0.42–1.55 wt%), Cr (0.82–2.66 ppm and 0.65–3.27 ppm), Co (0.23–0.62 ppm and 0.15–1.50 ppm) and Ni (0.43–1.74 ppm and 0.14–1.06 ppm) concentrations. They are all enriched in LREEs and LILEs, and depleted HREEs and HFSEs (Fig. 8). Combined with above geochemical features, we suggest the generation of Meiguifeng and Arxan plutons could be interpreted as the partial melting of crust materials. Moreover, the alkali feldspar granites from Meiguifeng pluton exhibit Nb/Ta ratios of 11.38–12.75 (with an average value of 11.75), and Zr/Hf ratios of 20.15–22.16 (with an average value of 21.48), which are closer to the corresponding ratios of crust (11.4 and 33, respectively; Taylor and McLennan, 1985) compared to primitive mantle (17.8 and 37, respectively; McDonough and Sun, 1995). The granite porphyries from Arxan pluton also have similar Nb/Ta (9.51–20.39; average=13.58) and Zr/Hf (20.80–33.96; average=27.96) ratios, which also provide effective evidences.

Based on above discussion, the granites from Meiguifeng and Arxan plutons were both originated from the partial melting of crust materials, with highly fractionated I-type granite affinity. Then, one question can be posed: What is the genetic relationship between them? Although the Meiguifeng and Arxan plutons were formed over a time span of about 10 Ma, their zircon grains possess relatively homogeneous Hf isotopic compositions. The Meiguifeng pluton show $^{176}Hf/^{177}Hf$ ratios of 0.282803–0.282969 and $\varepsilon_{Hf}(t)$ values of +4.04–+9.82, with T_{DM2} of 937–563 Ma, and the Arxan pluton have $^{176}Hf/^{177}Hf$ ratios varying from 0.282834 to 0.282965, with $\varepsilon_{Hf}(t)$ values of +4.93 to +9.57 and T_{DM2} of 870–574 Ma, indicating they were generated by juvenile crust materials. In addition, both of the samples from Meiguifeng and Arxan plutons plot in the field of experimental melts originated from medium- to high-K protoliths (Fig. 10a; Guo et al., 2012), suggesting that they were derived from medium- to high-K protoliths. Moreover, hydrous melting of basaltic rocks can produce peraluminous melts with high K contents (Beard and Lofgren, 1991; Chappell et al., 2012), and our samples all show weakly peraluminous characteristics (A/CNK=1.00–1.07) with high K_2O contents (4.58–4.98 wt%), indicating

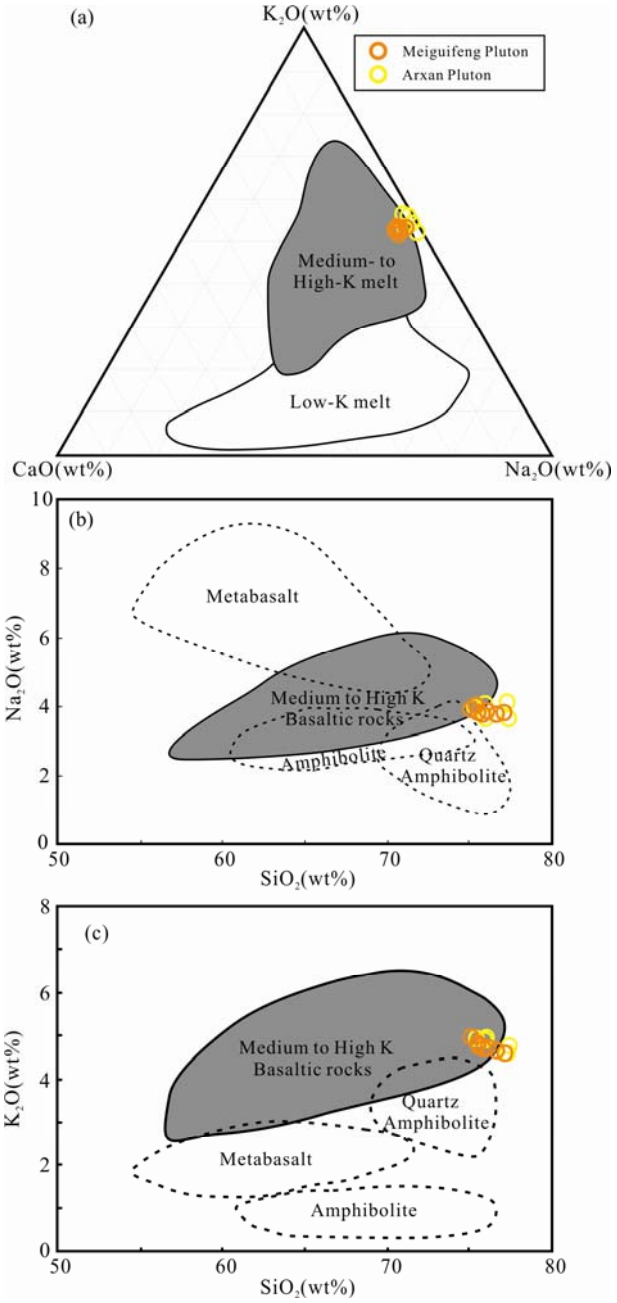

Fig. 10. (a) Ternary K_2O-Na_2O-CaO diagram (after Guo et al. 2012); (b) and (c) plots of Na_2O vs. SiO_2 and K_2O vs. SiO_2 for the Meiguifeng and Arxan plutons in Great Xing'an Range.

they were probably generated by partial melting of high-K basaltic crust. The diagrams of Na_2O vs. SiO_2 and K_2O vs. SiO_2 also provide important evidences for our above proposal (Figs. 10b and 10c). In summary, partial melting of Neoproterozoic high-K basaltic crust is the most likely process to generate magmas for Meiguifeng and Arxan plutons. Based on the petrological and geochemical characteristics of Meiguifeng and Arxan plutons, as well as their granite types, magma sources and petrogenetic processes, we suggest that they may share a common or similar magma source.

5.3 Tectonic implications

Our new and literature age data revealed impressive Early Cretaceous magmatism in the Great Xing'an Range, NE China, and the spatial distribution and temporal evolution can provide vital information on the tectonic evolution of CAOB. The studied Early Cretaceous Meiguifeng and Arxan plutons both belong to high-K calc-alkaline series (Fig. 7b), and their petrological and geochemical features show highly fractionated I-type granite affinity, with enrichment in LREEs and LILEs, and depletion in HREEs and HFSEs (Fig. 8). The generation of highly fractionated I-type granites could be associated with various tectonic environments including active continental margin and alternative post-collision extensional regime, as well as anorogenic setting (Wu et al., 2003; Li et al., 2007; Zhu et al., 2009). However, it is widely accepted that NE China was in an extensional environment during the Early Cretaceous, which is confirmed by the occurrence of metamorphic core complexes, extensional basins, bimodal volcanic rocks and A-type granites (Zhang et al., 1998, 2006; Ge et al., 1999, 2000, 2001; Shao et al., 2001; Wu et al., 2002; Meng, 2003; Fan et al., 2003; Gao et al., 2005; Tang et al., 2016; Li et al., 2018a). Over the last two decades, several geodynamic models have been proposed for the Late Mesozoic extension in NE China, including lithospheric extension after closure of Mongol-Okhotsk Ocean (Fan et al., 2003; Meng, 2003; Ying et al., 2010; Tang et al., 2016; Li et al., 2018a), lithospheric delamination or back-arc extension associated with the subduction of Paleo-Pacific Ocean (Wu et al., 2005, 2011; Wang et al., 2006; Zhang et al., 2010a, 2011; Sun et al., 2013a; Dong et al., 2014; Li et al., 2014, 2015a; Bar et al., 2018), and upwelling of the mantle plume (Lin et al., 1998; Ge et al., 2000; Deng et al., 2004). Combined with the temporal-spatial distribution, the formation of Early Cretaceous granitoid in NE China is inconsistent with the characteristics of mantle plume model, which is related to rapid and short-lived magmatism and circular distribution. Therefore, one question can be posed: What geodynamic mechanism was related to the generation of Early Cretaceous granitoid in NE China?

During the Mesozoic, NE China was controlled by the Mongol-Okhotsk and Paleo-Pacific tectonic regimes, implying a complex tectonic evolutionary history (Zhang et al., 2010a, b; Wu et al., 2011; She et al., 2012; Wang et al., 2012a, 2015; Shi et al., 2013, 2015; Xu et al., 2013a, b; Tian et al., 2015; Dong et al., 2014, 2016a, b; Li et al., 2014, 2015a, b, 2018a, b; Tang et al., 2014, 2016; Ji et al., 2016a, b, 2018a, 2019; He et al., 2017, 2018; Xie et al., 2017). The Mongol-Okhotsk suture zone extends for about 3000 km from central Mongolia northeastwards as far as the present-day Sea of Okhotsk (Chen et al., 2011; Tang et al., 2016; Dong et al., 2016b). The evolution of Mongol-Okhotsk Ocean can be traced back to Devonian, and it closed diachronously from west to east in the Mesozoic (Zorin, 1999; Kravchinsky et al., 2002; Cogné et al., 2005; Kelty et al., 2008; Donskaya et al., 2013; Sun et al., 2013b; Tang et al., 2016; Dong et al., 2016b). It was generally considered that the Mongol-Okhotsk oceanic plate was subducted northwards beneath the Siberian

Craton through the entire period of subduction (Zorin, 1999). However, some scholars regarded the northern margin of Mongolia-North China continent along the southern periphery of Mongol-Okhotsk Ocean as a passive margin during the Late Permian and later times (Chen et al., 2011; Wang et al., 2012a, 2015; Xu et al., 2013a, b; Tang et al., 2014, 2016), implying a southward subduction. Moreover, Tang et al. (2014) undertook zircon U-Pb dating, whole-rock geochemical analyses and Sr-Nd-Hf isotopic data of Triassic intrusive rocks in the Erguna Massif, and they concluded that the generation of Early-Middle Triassic magmatism in the Erguna Massif was associated with the southward subduction of Mongol-Okhotsk Ocean. However, the influence extent of Mongol-Okhotsk tectonic regime remains controversial, especially for its southward subduction (Xu et al., 2013a, b; Dong et al., 2014; Tang et al., 2014, 2016). Combined with spatial distribution and temporal evolution, as well as the tectonic evolution of Mongol-Okhotsk Ocean, Dong et al. (2016b) suggested that the Early Jurassic magmatism in Erguna Massif was controlled by the Mongol-Okhotsk tectonic regime, and the generation of Jurassic igneous rocks in the Xing'an Massif was probably related to the subduction of Paleo-Pacific Ocean. Therefore, it needs more effective measures to evaluate the relationship between Late Paleozoic-Mesozoic rocks in NE China and southward subduction of Mongol-Okhotsk Ocean and to determine the influence of Mongol-Okhotsk tectonic regime on NE China.

As for the Paleo-Pacific Ocean, it was originated from the Panthalassa, which was a vast global ocean during the Late Paleozoic-Mesozoic (Guo et al., 2016). The Paleo-Pacific plate includes three oceanic plates located at the same place as the present Pacific plate; they are Izanagi, Pheonix and Farallon plates. The Izanagi Plate is assumed to have underlain the Paleo-Pacific Ocean to the east of Eurasian continent. Meanwhile, workers have traced the tectonic history of Mudanjiang Ocean to Early Permian, which located between the Jiamusi and Songnen-Zhangguangcai Range massifs in NE China, and it closed in the Mesozoic (Ge et al., 2017; Zhu et al., 2017; Dong et al., 2018, 2019). The Mudanjiang Ocean should have played an important role in reconstructing the Mesozoic tectonic evolution of NE China, but its influence has been overlooked. Moreover, Ge et al. (2015, 2017) proposed that the Mudanjiang Ocean was probably a branch of Paleo-Pacific Ocean, and its subduction and closure may be linked to the evolution of Paleo-Pacific Ocean. Therefore, it is necessary to investigate the relation and mechanism of Mudanjiang Ocean and generation of Mesozoic igneous rocks in NE China.

In this study, combined with spatial distribution and temporal evolution, we assume that the formation of Early Cretaceous Meiguifeng and Arxan plutons in Xing'an Massif, Great Xing'an Range was closely related to the break-off of Mudanjiang oceanic plate. Based on geochronological and geochemical data from volcanic and sub-volcanic rocks in the Erlian Basin and adjacent areas, Tang et al. (2019) suggested that the Early Cretaceous extension in NE China was associated with the collapse of thickened lithosphere after the slab break-off of Mudanjiang Ocean and closure of Mongol-Okhotsk Ocean, providing supports for our proposal. Furthermore, compared with the Paleo-Pacific Ocean, the Mudanjiang Ocean was located closer to the Great Xing'an Range, and the seismological evidence shows that the influence of Paleo-Pacific Ocean did not reach the Great Xing'an Range in the Mesozoic (Zheng et al. 2015). However, researchers are motivated to connect the Early Cretaceous magmatism in Great Xing'an Range with the tectonic evolution of Paleo-Pacific Ocean, instead of Mudanjiang Ocean (Wu et al., 2005, 2011; Wang et al., 2006; Zhang et al., 2010a, 2011; Sun et al., 2013a; Dong et al., 2014; Li et al., 2014, 2015a; Bar et al., 2018). It is noteworthy that the Heilongjiang Complex contains greenschist, blueschist, amphibolite, serpentinite, muscovite-albite schist, two-mica schist, quartz schist (quartzite) and marble, which has been identified as either an ophiolitic mélange or a subduction-accretionary complex, representing the remnant of Mudanjiang Ocean (Ge et al., 2015, 2017; Zhu et al., 2015, 2017; Dong et al., 2018, 2019). Meanwhile, from a global perspective, some accretionary complex or ophiolitic mélange have been reported along the western Paleo-Pacific margin (Sivell and Waterhouse, 1988; Sano, 1992; Isozaki, 1997; Suzuki et al., 2005), implying that the Mudanjiang Ocean might be a part of the Paleo-Pacific Ocean.

6 Conclusions

Based on *in situ* zircon U-Pb-Hf isotopic data and whole-rock geochemical compositions from Meiguifeng and Arxan plutons, as well as regional geological characteristics, we draw the following conclusions:

(1) Zircon U-Pb geochronology indicates that the alkali feldspar granite from Meiguifeng pluton was emplaced at ~145 to 137 Ma, and the granite porphyry of Arxan pluton was formed at ~129 Ma, suggesting the Early Cretaceous magmatism occurred in the Xing'an Massif.

(2) The granites from Meiguifeng and Arxan plutons both show highly fractionated I-type granite affinity, and they may share a common or similar magma source. Partial melting of Neoproterozoic high-K basaltic crust is the most likely process to generate magmas for Meiguifeng and Arxan plutons.

(3) The generation of the Meiguifeng and Arxan pluton was closely related to the break-off of Mudanjiang oceanic plate. The Mudanjiang Ocean was probably a branch of Paleo-Pacific Ocean.

Acknowledgments

We thank Yang J.H. and Yang Y.H. for advice and assistance during in situ zircon U-Pb-Hf isotope analyses in the Institute of Geology and Geophysics, Chinese Academy of Sciences (Beijing), China. We appreciate the State Key Laboratory of Continental Dynamics, Northwest University, China, for their assistance in zircon U-Pb dating and whole-rock geochemical analyses. We thank the Beijing Research Institute of Uranium Geology, China for their assistance in whole-rock geochemical analyses. This study was financially supported by the National Key

R&D program of China (2016YFC0600403).

Manuscript received May 15, 2019
accepted Aug. 14, 2019
associate EIC XIAO Wenjiao
edited by LIU Lian

References

Andersen, T., 2002. Correction of common lead in U-Pb analyses that do not report ^{204}Pb. Chemical Geology, 192(1–2): 59–79.

Badarch, G., Cunningham, W.D., and Windley, B.F., 2002. A new terrane subdivision for Mongolia: implications for the Phanerozoic crustal growth of Central Asia. Journal of Asian Earth Sciences, 21(1): 87–110.

Barbarin, B., 1996. Genesis of the two main types of peraluminous granitoids. Geology, 24(4): 295–298.

Bars, A., Miao, L.C., Zhang, F.C., Baatar, M., Anaad, C., and Togtokh, K., 2018. Petrogenesis and tectonic implication of the Late Mesozoic volcanic rocks in East Mongolia. Geological Journal (doi.org/10.1002/gj.3080).

Beard, J., Lofgren, G., 1991. Dehydration melting and water-saturated melting of basaltic and andesitic greenstones and amphibolites at 1, 3, and 6. 9 kb. Journal of Petrology, 32(2): 365–401.

Bi, J.H., Ge, W.C., Yang, H., Zhao, G.C., Xu, W.L., and Wang, Z.H., 2015. Geochronology, geochemistry and zircon Hf isotopes of the Dongfanghong gabbroic complex at the eastern margin of the Jiamusi Massif, NE China: Petrogensis and tectonic implications. Lithos, 234: 27–46.

Blichert-Toft, J., Albarède, F., 1997. The Lu-Hf isotope geochemistry of chondrites and the evolution of the mantle-crust system. Earth and Planetary Science Letters, 148(1–2): 243–258.

Bonin, B., 2007. A-type granites and related rocks: evolution of a concept, problems and prospects. Lithos, 97(1–2): 1–29.

Cai, K.D., Sun, M., Yuan, C., Xiao, W.J., Zhao, G.C., Long, X.P., and Wu, F.Y., 2012. Carboniferous mantle-derived felsic intrusion in the Chinese Altai, NW China: Implications for geodynamic change of the accretionary orogenic Belt. Gondwana Research, 22(2): 681–698.

Cawthorn, R.G., Brown, P.A., 1976. A model for the formation and crystallization of corundum, -normative calc-alkaline magmas through amphibole fractionation. Journal of Geology, 84(4): 467–476.

Chappell, B.W., Bryant, C.J., and Wyborn, D., 2012. Peraluminous I-type granites. Lithos, 153: 142–153.

Chappell, B.W., White, A.J.R., 1974. Two contrasting granite types. Pacific Geology, 8: 173–174.

Chappell, B.W., White, A.J.R., 1992. I- and S-type granites in the Lachlan Fold Belt. Transactions of the Royal Society of Edinburgh: Earth Sciences, 83: 1–26.

Chappell, B.W., White, A.J.R., 2001. Two contrasting granite types: 25 years later. Australian Journal of Earth Sciences, 48 (4): 489–499.

Chen, Z.G., Zhang, L.C., Wan, B., Wu, H.Y., and Cleven, N., 2011. Geochronology and geochemistry of the Wunugetushan porphyry Cu-Mo deposit in NE China, and their geological significance. Ore Geology Reviews, 43(1): 92–105.

Chen, H.J., Zhang, Y.L., Wang, Q.H., Yang, H., Qian, C., Chen, J.S., Qin, T., Wang, Y., Wu, X.W., and Zhang, Y.J., 2015. Zircon U-Pb dating and geochemistry of the Early Cretaceous granitic rocks in the middle section of Daxinganling Mountains. Geology and Resources, 24: 433–443 (in Chinese with English abstract).

Cheng, R.Y., Wu, F.Y., Ge, W.C., Sun, D.Y., Liu, X.M., and Yang, J.H., 2006. Emplacement age of the Raohe Complex in eastern Heilongjiang Province and the tectonic evolution of the eastern part of northeastern China. Acta Petrologica Sincia, 22: 353–376 (in Chinese with English abstract).

Cogné, J.P., Kravchinsky, V.A., Halim, N., and Hankard, F., 2005. Late Jurassic-Early Cretaceous closure of the Mongol-Okhotsk Ocean demonstrated by new Mesozoic palaeomagnetic results from the Trans-Baikal area (SE Siberia). Geophysical Journal International, 163: 813–832.

Collins, W.J., Beams, S.D., White, A.J.R., and Chappell, B.W., 1982. Nature and origin of A-type granites with particular reference to southeastern Australia. Contributions to Mineralogy and Petrology, 80(2): 189–200.

Deng, J.F., Mo, X.X., Zhao, H.L., Wu, Z.X., Luo, Z.H., and Su, S.G., 2004. A new model for the dynamic evolution of Chinese lithosphere: 'continental roots–plume tectonics'. Earth Science Reviews, 65(3–4): 223–275.

Dong, Y., Ge, W.C., Yang, H., Zhao, G.C., Wang, Q.H., Zhang, Y.L., and Su, L., 2014. Geochronology and geochemistry of Early Cretaceous volcanic rocks from the Baiyingaolao Formation in the central Great Xing'an Range, NE China, and its tectonic implications. Lithos, 205: 168–184.

Dong, Y., Ge, W.C., Yang, H., Ji, Z., Wang, Z.H., Bi, J.H., and Zhu, Y., 2016a. Petrogenesis of Early Cretaceous granodiorite-porphyry from Huanan area in eastern Heilongjiang and its geological implication. Global Geology, 35: 617–640 (in Chinese with English abstract).

Dong, Y., Ge, W.C., Yang, H., Xu, W.L., Zhang, Y.L., Bi, J.H., and Liu, X.W., 2016b. Geochronology, geochemistry, and Hf isotopes of Jurassic intermediate-acidic intrusions in the Xing'an Block, northeastern China: Petrogenesis and implications for subduction of the Paleo-Pacific oceanic plate. Journal of Asian Earth Sciences, 118: 11–31.

Dong, Y., Ge, W.C., Zhao, G.C., Yang, H., Liu, X.W., and Zhang, Y.L., 2016c. Petrogenesis and tectonic setting of the Late Paleozoic Xing'an complex in the northern Great Xing'an Range, NE China: Constraints from geochronology, geochemistry and zircon Hf isotopes. Journal of Asian Earth Sciences, 115: 228–246.

Dong, Y., Ge, W.C., Yang, H., Ji, Z., He, Y., Zhao, D., and Xu, W.L., 2018. Convergence history of the Jiamusi and Songnen-Zhangguangcai Range massifs: Insights from detrital zircon U -Pb geochronology of the Yilan Heilongjiang Complex, NE China. Gondwana Research, 56: 51–68.

Dong, Y., Ge, W.C., Yang, H., Liu, X.W., Bi, J.H., Ji, Z., and Xu, W.L., 2019. Geochemical and SIMS U-Pb rutile and LA-ICP-MS U-Pb zircon geochronological evidence of the tectonic evolution of the Mudanjiang Ocean from amphibotites of the Heilongjiang Complex, NE China. Gondwana Research, 69: 25–44.

Donskaya, T.V., Gladkochub, D.P., Mazukabzov, A.M., and Ivanov, A.V., 2013. Late Paleozoic-Mesozoic subduction-related magmatism at the southern margin of the Siberian continent and the 150 million-year history of the Mongol-Okhotsk Ocean. Journal of Asian Earth Sciences, 62: 79–97.

Eby, G.N., 1990. The A-type granitoids: a review of their occurrence and chemical characteristics and speculations on their petrogenesis. Lithos, 26(1–2): 115–134.

Eby, G.N., 1992. Chemical subdivision of the A-type granitoids: petrogenetic and tectonic implications. Geology, 20: 641–644.

Fan, W.M., Guo, F., Wang, Y.J., and Lin, G., 2003. Late Mesozoic Calc-alkaline Volcanism of Post-orogenic Extension in the Northern Da Hinggan Mountains, Northeastern China. Journal of Volcanology and Geothermal Research, 121(1–2): 115–135.

Gao, X.F., Guo, F., Fan, W.M., Li, C.W., and Li, X.Y., 2005. Origin of Late Mesozoic Intermediate-felsic Volcanic Rocks from the Northern Da Hinggan Mountain, NE China. Acta Petrologica Sinica, 21: 737–748 (in Chinese with English abstract).

Gao, Y., Zheng, C.Q., Yao, W.G., Wang, H., Li, J., Shi, L., Cui, F.H., Gao, F., and Zhang, X.X., 2013. Geochemistry and zircon U-Pb geochronology of the Luotuobozi Pluton in the Haduohe Area in the northern Daxing'anling. Acta Geologica Sinica, 87: 1293–1310 (in Chinese with English abstract).

Ge, W.C., Lin, Q., Sun, D.Y., Wu, F.Y., Yuan, Z.K., Li, W.Y., Chen, M.Z., and Yin, C.X, 1999. Geochemical Characteristics of the Mesozoic Basalts in Da Hinggan Ling: Evidence of the Mantle-crust Interaction. Acta Petrologica Sinica, 15: 396–406 (in Chinese with English abstract).

Ge, W.C., Lin, Q., Sun, D.Y., Wu, F.Y., and Li, X.H., 2000. Geochemical Research into Origins of Two Types of Mesozoic Rhyolites in Daxing'anling. Earth Science-Journal of China University of Geosciences, 25: 172–178 (in Chinese

with English abstract).
Ge, W.C., Li, X.H., Lin, Q., Sun, D.Y., Wu, F.Y., and Yin, C.X., 2001. Geochemistry of Early Cretaceous Alkaline Rhyolites from Hulun lake, Daxinganling and its Tectonic Implications. Scientia Geologica Sinica, 36: 176–183 (in Chinese with English abstract).
Ge, W.C., Wu, F.Y., Zhou, C.Y., and Zhang, J.H., 2005. Zircon U-Pb ages and its significance of the Mesozoic granites in the Wulanhaote region, central Da Hinggan Mountain. Acta Petrologica Sinica, 21: 749–762 (in Chinese with English abstract).
Ge, M.H., Zhang, J.J., Liu, K., Ling, Y.Y., Wang, M., and Wang, J.M., 2015. Geochemistry and geochronology of the blueschist in the Heilongjiang Complex and its implications in the late Paleozoic tectonics of eastern NE China. Lithos, 261: 232–249.
Ge, M.H., Zhang, J.J., Li, L., Liu, K., Ling, Y.Y., Wang, J.M., and Wang, M., 2017. Geochronology and geochemistry of the Heilongjiang Complex and the granitoids from the Lesser Xing'an-Zhangguangcai Range: Implications for the late Paleozoic-Mesozoic tectonics of eastern NE China. Tectonophysics, 717: 565–584.
Guo, F., 2016. Geological records of the Pacific Plate subduction in the northeast Aisan continental margin: an overview. Bulletin of Mineralogy, Petrology and Geochemistry, 35: 1082–1089 (in Chinese with English abstract).
Guo, F., Fan, W.M., Li, C.W., Zhao, L., Li, H.X., and Yang, J.H., 2012. Multi-stage crust-mantle interaction in SE China: temporal, thermal and compositional constraints from the Mesozoic felsic volcanic rocks in eastern Guangdong-Fujian provinces. Lithos, 150: 62–84.
Harris, N.B.W., Inger, S., and Ronghua, X., 1990. Cretaceous plutonism in Central Tibet: an example of post-collision magmatism?. Journal of Volcanology and Geothermal Research, 44(1–2): 21–32.
He, Y., Dong, Y., He, Z.H., Zhang, Y.L., Yang, H., Wang, Q.H., and Chen, H.J., 2017. Petrogenesis of Early Cretaceous Ailinyuan granites from northern-central Da Hinggan mountains: constraints from zircon U-Pb age, geochemistry and Hf isotopes. Global Geology, 36: 701–713 (in Chinese with English abstract).
He, Y., He, Z.H., Ge, W.C., Yang, H., Wang, Z.H., Dong, Y., Bi, J.H., and Zhao, D., 2018. Petrogenesis and tectonic implications of Late Jurassic-Early Cretaceous granitic magmatism in the Xing'an Block, northeast China: geochronological, geochemical, and Hf isotopic evidence. Canadian Journal of Earth Sciences, 55(6): 571–588.
IMBGMR (Inner Mongolian Bureau of Geology Mineral Resources), 1991. Regional Geology of Inner Mongolia. Geological Publishing House, Beijing.
Irvine, T.N., Baragar, W.R.A., 1971. A Guide to the Chemical Classification of the Common Volcanic Rocks. Canadian Journal of Earth Sciences, 8(5): 523–548.
Isozaki, Y., 1997. Contrasting two types of orogen in Permo-Triassic Japan: Accretionary versus collisional. Island Arc, 6 (1): 2–24.
Jahn, B.M., Wu, F.Y., and Chen, B., 2000. Massive granitoid generation in Central Asia: Nd isotope evidence and implication for continental growth in the Phanerozoic. Episodes, 23: 82–92.
Jahn, B.M., Capdevila, R., Liu, D., Vernov, A., and Badarch, G., 2004. Sources of Phanerozoic granitoids in the transect Bayanhongor-Ulan Baator, Mongolia: geochemical and Nd isotopic evidence, and implications of Phanerozoic crustal growth. Journal of Asian Earth Sciences, 23: 629–653.
Jahn, B.M., Litvinovsky, B.A., Zanvilevich, A.N., and Reichow, M., 2009. Peralkaline granitoid magmatism in the Mongolian-Transbaikalian Belt: evolution, petrogenesis and tectonic significance. Lithos, 113: 521–539.
Ji, Z., Ge, W.C., Yang, H., Tian, D.X., Zhang, Y.L., and Chen, H.J., 2016a. Petrogenesis of Early Cretaceous granites in Taerqi area of central Great Xing'an Range and its tectonic setting. Global Geology, 35: 283–296 (in Chinese with English abstract).
Ji, Z., Ge, W.C., Wang, Q.H., Yang, H., Zhao, G.C., Bi, J.H., and Dong, Y., 2016b. Petrogenesis of Early Cretaceous volcanic rocks of the Manketouebo Formation in the Wuchagou region, central Great Xing'an Range, NE China, and tectonic implications: geochronological, geochemical, and Hf isotopic evidence. International Geology Review, 58(5): 556–573.
Ji, Z., Ge, W.C., Yang, H., Tian, D.X., Chen, H.J., and Zhang, Y.L., 2018b. Late Carboniferous-Early Permian high- and low -Sr/Y granitoids of the Xing'an Block, northeastern China: Implications for the late Paleozoic tectonic evolution of the eastern Central Asian Orogenic Belt. Lithos, 322: 179–196.
Ji, Z., Ge, W.C., Yang, H., Wang, Q.H., Zhang, Y.L., Wang, Z.H., Bi, J.H., 2018a. Late Jurassic rhyolites from the Wuchagou region in the central Great Xing'an Range, NE China: petrogenesis and tectonic implications. Journal of Asian Earth Sciences, 158: 381-397.
Ji, Z., Meng, Q.A., Wan, C.B., Ge, W.C., Yang, H., Zhang, Y.L., Dong, Y., and Jin, X., 2019. Early Cretaceous adakitic lavas and A-type rhyolites in the Songliao Basin, NE China: Implications for the mechanism of lithospheric extension. Gondwana Research, 71: 28–48.
Jiang, H., Li, W.Q., Jiang, S.Y., Wang, H., and Wei, X.P., 2017. Geochronological, geochemical and Sr-Nd-Hf isotopic constraints on the petrogenesis of Late Cretaceous A-type granites from the Sibumasu Block, Southern Myanmar, SE Asia. Lithos, 268–271: 32–47.
Kelty, T.K., Yin, A., Dash, B., Gehrels, G.E., and Ribeiro, A.E., 2008. Detrital-zircon geochronology of Paleozoic sedimentary rocks in the Hangay-Hentey basin, north-central Mongolia: implications for the tectonic evolution of the Mongol–Okhotsk Ocean in central Asia. Tectonophysics, 451: 290–311.
King, P.L., White, A.J.R., Chappell, W., and Allen, C.M., 1997. Characterization and origin of aluminous A-type granites from the Lachlan Fold Belt, Southeastern Australia. Journal of Petrology 38(3): 371–391.
Koschek, G., 1993. Origin and significance of the SEM cathodoluminescence from zircon. Journal of Microscopy, 171 (3): 223–232.
Kravchinsky, V.A., Cogné, J.P., Harbert, W.P., and Kuzmin, M.I., 2002. Evolution of the Mongol-Okhotsk Ocean as constrained by new palaeomagnetic data from the Mongol-Okhotsk suture zone, Siberia. Geophysical Journal International, 148(1): 34 – 57.
Li, J.Y., 2006. Permian geodynamic setting of northeast China and adjacent regions: closure of the Paleo-Asian ocean and subduction of the Paleo-Pacific plate. Journal of Asian Earth Sciences, 26(3–4): 207–224.
Li, X.H., Li, Z.X., Li, W.X., Liu, Y., Yuan, C., Wei, G., and Qi, C., 2007. U-Pb zircon, geochemical and Sr-Nd-Hf isotopic constraints on age and origin of Jurassic I-and A-type granites from central Guangdong, SE China: a major igneous event in response to foundering of a subducted flflat-slab?. Lithos, 96: 186–204.
Li, S.Q., Hegner, E., Yang, Y.Z., Wu, J.D., and Chen, F.K., 2014. Age constraints on late Mesozoic lithospheric extension and origin of bimodal volcanic rocks from the Hailar basin, NE China. Lithos, 190: 204–219.
Li, S.Q., Yang, Y.Z., Xie, Q.L., Wang, Y., and Chen, F.K., 2015a. Age constraints on late Mesozoic lithospheric extension and origin of felsic volcanism in the Songliao basin, NE China. The Journal of Geology, 123(2): 153–175.
Li, Y., Ding, L.L., Xu, W.L., Wang, F., Tang, J., Zhao, S., and Wang, Z.J., 2015b. Geochronology and geochemistry of muscovite granite in Sunwu area, NE China: Implications for the timing of closure of the Mongol-Okhotsk Ocean. Acta Petrologica Sinica, 31: 56–66 (in Chinese with English abstract).
Li, Y., Xu, W.L., Tang, J., Pei, F.P., Wang, F., and Sun, C.Y., 2018a. Geochronology and geochemistry of Mesozoic intrusive rocks in the Xing'an Massif of NE China: Implications for the evolution and spatial extent of the Mongol-Okhotsk tectonic regime. Lithos, 304–307: 57–73.
Li, Y.L., Liu, H.C., Huangfu, P.P., He, H.Y., and Liu, Y.Z., 2018b. Early Cretaceous lower crustal reworking in NE China: insights from geochronology and geochemistry of felsic

igneous rocks from the Great Xing'an Range. International Journal of Earth Sciences, 107: 1955–1974.
Lin, Q., Ge, W.C., Sun, D.Y., Wu, F.Y., Chong, K.W., Kyung, D.M., Myung, S.J., Moon, W.W., Chi, S.K., and Sung, H.Y., 1998. Tectonic signifificance of Mesozoic volcanic rocks in northeastern China. Scientia Geologica Sinica, 33: 129–139 (in Chinese with English abstract).
Liu, Y.J., Li, W.M., Feng, Z.Q., Wen, Q.B., Neubauer, F., and Liang, C.Y., 2017. A review of the Paleozoic tectonic in the eastern part of Central Asian Orogenic Belt. Gondwana Research, 43: 123–148.
Loiselle, M.C., and Wones, D.S., 1979. Characteristics and origin of anorogenic granites. Geological Society of America, 11: 468.
Ludwig, K.R., 2003. User's manual for Isoplot 3.00: a geochronological toolkit for Microsoft Excel. Berkeley Geochronology Center Special Publication, 4: 1–70.
Maniar, P.D., and Piccoli, P.M., 1989. Tectonic discrimination of granitoids. Geological Society of American Bulletin, 101: 635–643.
McDonough, W.F., and Sun, S.S., 1995. The Composition of the Earth. Chemical Geology, 120: 223–253.
Meng, Q.R., 2003. What drove late Mesozoic extension of the northern China-Mongolia tract?. Tectonophysics, 369: 155–174.
Miao, L.C., Fan, W.M., Zhang, F.Q., Liu, D.Y., Jian, P., Shi, G.H., Tao, H., and Shi, Y.R., 2004. Zircon SHRIMP geochronology of the Xinkailing-Kele complex in the Northwestern Lesser Xing'an Range, and its geological implications. Chinese Science Bulletin, 49: 201–209.
Miao, L.C., Liu, D.Y., Zhang, F.Q., Fan, W.M., Shi, Y.R., and Xie, H.Q., 2007. Zircon SHRIMP U-Pb ages of the "Xinghuadukou Group" in Hanjiayuanzi and Xinlin areas and the "Zhalantun Group" in Inner Mongolia, Da Hinggan Mountains. Chinese Science Bulletin, 52: 1112–1134.
Miller, C.F., 1985. Are strongly peraluminous magmas derived from politic sedimentary sources?. Journal of Geology, 93: 673–689.
Peccerillo, A., Taylor, S.R., 1976. Geochemistry of eocene calc–alkaline volcanic rocks from the Kastamonu area, Northern Turkey. Contributions to Mineralogy and Petrology, 58(1): 63–81.
Pitcher, W.S., 1982. Granite type and tectonic environment, in Hsu, K.J. (ed.), Mountain Building Processes, Academic Press, London: 19–40.
Pupin., J.P., 1980. Zircon and granite petrology. Contributions to Mineralogy and Petrology, 73: 207–220.
Safonova, I.Yu., Santosh, M., 2014. Accretionary complexes in the Asia-Pacific region: tracing archives of ocean plate stratigraphy and tracking mantle plumes. Gondwana Research, 25: 126–158.
Sano, S., 1992. Neodymium isotopic compositions of Silurian Yakuno metagabbros. Journal of Mineralogy Petrology & Economic Geology, 87: 272–282.
Scherer E E, Munker C, and Mezger K, 2001. Calibration of the Lutetium-hafnium clock. Science, 293: 683–687.
Shao, J.A., Liu, F.T., Chen, H., and Han, Q.J., 2001. Relationship between Mesozoic Magmatism and Subduction in Da Hinggan-Yanshan Area. Acta Geologica Sinica, 75: 56–63 (in Chinese with English abstract).
She, H.Q., Li, J.W., Xiang, A.P., Guan, J.D., Zhang, D.Q., Yang, Y.C., Tan, G., and Zhang, B., 2012. U-Pb ages of the zircons from primary rocks in middle-northern Daxinganling and its implications to geotectonic evolution. Acta Petrologica Sinca, 28: 571–594 (in Chinese with English abstract).
Shi, L., 2015. Late Mesozoic magmatism and tectonic setting in Chaihe-Moguqi region, central Great Xing'an Range: Jilin University (in Chinese with English abstract).
Shi, L., Zheng, C.Q., Yao, W.G., Li, J., Xu, J.L., Gao, Y., and Cui, F.H., 2013. Geochronology, petro-geochemistry and tectonic setting of the Hamagou Forest Farm A-type granites in the Wuchagou Region, central Great Xinggan Range. Acta Geologica Sinica, 87: 1264–1276 (in Chinese with English abstract).
Shi, L., Zheng, C.Q., Yao, W.G., Li, J., Cui, F.H., Gao, F., Gao, Y., Xu, J.L., and Han, X.M., 2015. Geochronological framework and tectonic setting of the granitic magmatism in the Chaihe-Moguqi region, central Great Xing'an Range, China. Journal of Asian Earth Sciences, 113: 443–453.
Sivell, W.J., Waterhouse, J.B., 1988. Petrogenesis of Gympie Group volcanics: evidence for remnants of an early Permian volcanic arc in eastern Australia. Lithos, 21: 81–95.
Sun, D.Y., Wu, F.Y., Gao, S., and Lu, X.P., 2005. Confirmation of two episodes of A-type granite emplacement during Late Triassic and Early Jurassic in the central Jilin Province, and their constraints on the structural pattern of the east Jilin-Heilongjiang area, China. Earth Science Frontiers, 12: 263–275 (in Chinese with English abstract).
Sun, M.D., Chen, H.L., Zhang, F.Q., Wilde, S.A., Dong, C.W., and Yang, S.F., 2013a. A 100 Ma bimodal composite dyke complex in the Jiamusi Block, NE China: an indication for lithospheric extension driven by Paleo-Pacifific roll-back. Lithos, 162–163: 317–330.
Sun, D.Y., Gou, J., Wang, T.H., Ren, Y.S., Liu, Y.J., Guo, H.Y., Liu, X.M., and Hu, Z.C., 2013b. Geochronological and geochemical constraints on the Erguna massif basement, NE China-subduction history of the Mongol-Okhotsk oceanic crust. International Geology Review, 55: 1801–1816.
Suzuki, N., Kojima, S., Kano, H., Yamakita, S., Misaki, A., Ehiro, M., Otoh, S., Kurihara, T., and Aoyama, M., 2005. Permian radiolarian faunas from chert in the Khabarovsk Complex, Far East Russia, and the age of each lithological unit of the Khabarovsk Complex. Journal of Paleontology, 79: 686–700.
Tang, J., Xu, W.L., Wang, F., Wang, W., Xu, M.J., and Zhang, Y.H., 2014. Geochronology and geochemistry of Early-Middle Triassic magmatism in the Erguna Massif, NE China: constraints on the tectonic evolution of the Mongol-Okhotsk Ocean. Lithos, 184: 1–16.
Tang, J., Xu, W.L., Wang, F., Zhao, S., and Wang, W., 2016. Early Mesozoic southward subduction history of the Mongol-Okhotsk oceanic plate: Evidence from geochronology and geochemistry of Early Mesozoic intrusive rocks in the Erguna Massif, NE China. Gondwana Research, 31: 218–240.
Tang, J.Z., Zhang, Z.C., Ji, Z.J., Chen, Y., Li, K., Yang, J.F., and Liu, P.P., 2019. Early Cretaceous volcanic and sub-volcanic rocks in the Erlian Basin and adjacent areas, northeast China: new geochemistry, geochronology and zircon Hf isotope constraints on petrogenesis and tectonic setting. International Geology Review, 61(12): 1479–1503.
Taylor, S.R., McLennan, S.M., 1985. The Continental Crust: Its Composition and Evolution, Blackwell, Oxford Press.
Tian, D.X., Ge, W.C., Yang, H., Zhao, G.C., and Zhang, Y.L., 2015. Lower Cretaceous alkali feldspar granites in the central part of the Great Xing'an Range, northeastern China: Chronology, geochemistry and tectonic implications. Geological Magazine, 152(3): 383–399.
Veevers, J.J., Saeed A, Belousova E A, and Griffin WL., 2005. U-Pb ages and source composition by Hf-isotope and trace-element analysis of detrital zircons in Permian sandstone and modern sand from southwestern Australia and a review of the paleogeographical and denudational history of the Yilgarn Craton. Earth Science Reviews, 68(3–4): 245–279.
Wang, F., Zhou, X.H., Zhang, L.C., Ying, J.F., Zhang, Y.T., Wu, F.Y., and Zhu, R.X., 2006. Late Mesozoic volcanism in the Great Xing'an Range (NE China): timing and implications for the dynamic setting of NE Asia. Earth and Planetary Science Letters, 251(1–2): 179–198.
Wang, W., Xu, W.L., Wang, F., and Meng, E., 2012a. Zircon U-Pb chronology and assemblages of Mesozoic granitoids in the Manzhouli-Erguna area, NE China: Constraints on the regional tectonic evolution. Geological Journal of China Universities, 18: 88–105 (in Chinese with English abstract).
Wang, X.A., Xu, Z.Y., Liu, Z.H., and Zhu, K., 2012b. Petrogenesis and tectonic setting of the K-feldspar granites in Chaihe area, central Greater Xing'an Range: Constraints from petro-geochemistry and zircon U-Pb isotope chronology. Acta Petrologica Sinca, 28: 2647–2655 (in Chinese with English abstract).
Wang, W., Tang, J., Xu, W.L., and Wang, F., 2015.

Geochronology and geochemistry of Early Jurassic volcanic rocks in the Erguna Massif, northeast China: Petrogenesis and implications for the tectonic evolution of the Mongol-Okhotsk suture belt. Lithos, 218–219: 73–86.

Wang, Y.L., Ao, G., Wang, H.P., Wang, Z.J., Wang, Q., Zhong, M.S., Tan, C., Yang, Y.L., Li, Z., Niu, M.W., and Ke, K.J., 2019. Zircon U-Pb geochronology, geochemistry and tectonic significance of Early Cretaceous granites in Suolun area of central Da Hinggan Mountains. Geological Science and Technology Information, 38: 45–57 (in Chinese with English abstract).

Whalen, J.B., Currie, K.L., and Chappell, B.W., 1987. A-type granites: geochemical characteristics, discrimination and petrogenesis. Contributions to Mineralogy and Petrology, 95 (4): 407–419.

Wilde, S.A., Wu, F.Y., and Zhao, G.C., 2010. The Khanka Block, NE China, and its significance to the evolution of the Central Asian Orogenic Belt and continental accretion, in Kusky, T.M., Zhai, M.G., Xiao, W.J., eds, The Evolving Continents: Understanding Processes of Continental Growth. Geological Society, London, Special Publication, 338: 117–137.

Wolf, M.B., and London, D., 1994. Apatite dissolution into peraluminous haplogranite melts: an experimental study of solubilities and mechanisms. Geochimica et Cosmochimica Acta, 58(19): 4127–4145.

Wu, F.Y., Jahn, B.M., Wilde, S., and Sun, D.Y., 2000. Phanerozoic continental crustal growth: Sr-Nd isotopic evidence from the granites in northeastern China. Tectonophysics, 328: 89–113.

Wu, F.Y., Sun, D.Y., Li, H.M., Jahn, B.M., and Wilde, S.A., 2002. A-type granites in northeastern China: age and geochemical constraints on their petrogenesis. Chemical Geology, 187: 143–173.

Wu, F.Y., Jahn, B.M., Wilde, S.A., Lo, C.H., Yui, T.F., Lin, Q., and Sun, D.Y., 2003. Highly fractionated I-type granites in NE China (II): isotopic geochemistry and implications for crustal growth in the Phanerozoic. Lithos, 67: 191–204.

Wu, F.Y., Yang, J.H., Wilde, S.A., and Zhang, X.O., 2005. Geochronology, petrogenesis and tectonic implications of Jurassic granites in the Liaodong Peninsula, NE China. Chemical Geology, 221: 127–156.

Wu, F.Y., Yang, Y.H., Xie, L.W., Yang, J.H., and Xu, P., 2006. Hf isotopic compositions of the standard zircons and baddeleyites used in U-Pb Geochronology. Chemical Geology, 234: 105–126.

Wu, F.Y., Sun, D.Y., Ge, W.C., Zhang, Y.B., Grant, M.L., Wilde, S.A., and Jahn, B.M., 2011. Geochronology of the Phanerozoic granitoids in northeastern China. Journal of Asian Earth Sciences, 41: 1–30.

Wu, C., Jiang, T., Liu, W.C., Zhang, D., and Zhou, Z.G., 2015. Early Cretaceous adakitic and mineralization of the Yili porphyry Mo deposit in the Great Xing'an Range: implications for the geodynamic evolution of northeastern China. International Geology Review, 57(9–10): 1152–1171.

Wyborn, D., Turner, B.S., and Chappell, B.W., 1987. The Boggy Plain Supersuite: a distinctive belt of I-type igneous rocks of potential economic significance in the Lachlan Fold Belt. Australian Journal of Earth Sciences, 34(1): 21–43.

Wyborn, D., Chappell, B.W., and James, M., 2001. Examples of convective fractionation in high temperature granites from the Lachlan Fold Belt. Australian Journal of Earth Sciences, 48 (4): 531–541.

Xiao, W.J., Santosh, M., 2014. The western Central Asian Orogenic Belt: A window to accretionary orogenesis and continental growth. Gondwana Research, 25: 1429–1444.

Xie, J., Ge, W.C., Ji, Z., Wang, Q.H., Yang, H., and He, Y., 2017. Geochemical characteristic and petrogenesis of Early Cretaceous granitoids in Wuchagou region of central Great Xing'an Range. Global Geology, 36: 22–40 (in Chinese with English abstract).

Xu, W.L., Pei, F.P., Wang, F., Meng, E., Ji, W.Q., Yang, D.B., and Wang, W., 2013a. Spatial-temporal relationships of Mesozoic volcanic rocks in NE China: constraints on tectonic overprinting and transformations between multiple tectonic regimes. Journal of Asian Earth Sciences, 74: 167–193.

Xu, W.L., Wang, F., Pei, F.P., Meng, E., Tang, J., Xu, M.J., and Wang, W., 2013b. Mesozoic tectonic regimes and regional ore-forming background in NE China: Constrains from spatial and temporal variations of Mesozoic volcanic rock associations. Acta Petrologica Sinica, 29: 339–353 (in Chinese with English abstract).

Xu, L.M., Wang, D.K., Liu, Y., Zheng, J.L., Zhang, W.Q., and Liang, Z.K., 2018. Age and geochemistry of the Early Cretaceous intrusive rocks in southern Tahe, northern Great Xing'an Range. Geoscience, 32: 1212–1226 (in Chinese with English abstract).

Yang, J.H., Wu, F.Y., Shao, J.A., Wilde, S.A., Xie, L.W., and Liu, X.M., 2006. Constrains on the timing of uplift of the Yanshan Fold and Thrust Belt, north China. Earth and Planetary Science Letters, 246(3–4): 336–352.

Yin, Z.G., Gong, Z.M., Zhang, Y.L., Han, Y., Wang, Y., Cao, Z.Q., Li, H.N., and Li, M., 2018. Geochronology, geochemistry and geological significance of the Early Cretaceous alkali feldspar granites in the Yilehuli Mountain, Da Hinggan, Mountain. Geological Bulletin of China, 37: 1061–1074 (in Chinese with English abstract).

Ying, J.F., Zhou, X.H., Zhang, L.C., and Wang, F., 2010. Geochronological framework of Mesozoic volcanic rocks in the Great Xing'an Range, NE China, and their geodynamic implications. Journal of Asian Earth Sciences, 39: 786–793.

Yu, J.J., Liu, J.C., Zhang, J.H., Ge, W.C., and Hou, X.G., 2013a. Zircon U-Pb dating of the granodiorite-porphyries in Jiejinkou-Fuyuan area, northeastern Heilongjiang Province and its geological significance. Journal of Jilin University (Earth Science Edition), 43: 1489–1500 (in Chinese with English abstract).

Yu, J.J., Zhang, Y.L., Ge, W.C., and Yang, H., 2013b. Geochronology and geochemistry of the Late Cretaceous granitoids in the northern margin of the Sanjiang basin, NE China and its tectonic implications. Acta Petrologica Sinica, 29: 369–385 (in Chinese with English abstract).

Yu, Q., Ge, W.C., Yang, H., Zhao, G.C., Zhang, Y.L., and Su, L., 2014. Petrogenesis of Late Paleozoic Volcanic Rocks from the Daheshen Formation in Central Jilin Province, NE China, and Its Tectonic Implications: Constraints from Geochronology, Geochemistry and Sr–Nd–Hf Isotopes. Lithos, 192–195: 116–131.

Yu, Q., 2017. Petrogenesis of the Late Paleozoic-Early Mesozoic intrusive rocks in the Xing'an Terrane, and its geological implication. Jilin University (in Chinese with English abstract).

Yu, Q., Ge, W.C., Zhang, J., Zhao, G.C., Zhang, Y.L., and Yang, H., 2017. Geochronology and petrogenesis and tectonic implications of Late Paleozoic volcanic rocks from the Dashizhai Formation in Inner, Mongolia, NE China. Gondwana Research, 43: 164–177.

Zhang, J.H., 2006. Geochronological Framework of the Mesozoic Volcanic Rocks in the Great Xing'an Range, NE China. Jilin University (in Chinese with English abstract).

Zhang, J.H., 2009. Geochronology and Geochemistry of the Mesozoic Volcanic rocks in the Great Xing'an Range, Northeastern China. China University of Geoscience (in Chinese with English abstract).

Zhang, L.Q., Shao, J.A., and Zheng, G.R., 1998. Metamorphic Core Complex in Ganzhuermiao Inner Mongolia. Scientia Geologica Sinica, 33: 14–20 (in Chinese with English abstract).

Zhang, Y.L., Ge, W.C., Liu, X.M., and Zhang, J.H., 2008. Isotopic Characteristics and Its Significance of the Xinlin Town Pluton, Great Hinggan Mountains. Journal of Jilin University (Earth Science Edition), 38: 177–186 (in Chinese with English abstract).

Zhang, J.H., Gao, S., Ge, W.C., Wu, F.Y., Yan, J.H., Wilde, S.A., and Li, M., 2010a. Geochronology of the Mesozoic volcanic rocks in the Great Xing'an Range, northeastern China: Implications for subduction-induced delamination. Chemical Geology, 276(3–4): 144–165.

Zhang, Y.L., Ge, W.C., Gao, Y., Chen, J.S., and Zhao, L., 2010b. Zircon U-Pb ages and Hf isotopes of granites in Longzhen

area and their geological implications. Acta Petrologica Sinica, 26: 1059–1073 (in Chinese with English abstract).
Zhang, F.Q., Chen, H.L., Yu, X., Dong, C.W., Yang, S.F., Pang, Y.M., and Batt, G.E., 2011. Early Cretaceous volcanism in the northern Songliao Basin, NE China, and its geodynamic implication. Gondwana Research, 19: 163–176.
Zhang, Y.T., Sun, F.Y., Wang, S., and Xin, W., 2018. Geochronology and geochemistry of Late Jurassic to Early Cretaceous granitoid in the northern Great Xing'an Range, NE China: Petrogenesis and implications for late Mesozoic tectonic evolution. Lithos, 312–313: 171–185.
Zhao, Z., 2011. Late Paleozoic magmatism and its tectonic significance in the northern Great Xing'an Range, northeastern China. Jilin University (in Chinese with English abstract).
Zheng, T.Y., He, Y.M., Yang, J.H., and Zhao, L., 2015, Seismological constraints on the crustal structures generated by continental rejuvenation in northeastern China. Scientific Report, 5: 14995.
Zhou, Y., Ge, W.C., and Wang, Q.H., 2011. Petrogenesis of Mesozoic Granite in Wulanhaote Region, Central Da Hinggan Mountains. Constraints from Geochemistry and Sr-Nd-Hf isotope: Acta Petrologica ET Mineralogica, 30: 901–923 (in Chinese with English abstract).
Zhu, D.C., Mo, X.X., Wang, L.Q., Zhao, Z.D., Niu, Y.L., Zhou, C.Y., and Yang, Y.H., 2009. Petrogenesis of highly fractionated I-type granites in the Zayu area of eastern Gangdese, Tibet: Constraints from zircon U-Pb geochronology, geochemistry and Sr-Nd-Hf isotopes. Science in China (Earth Sciences), 52: 1223–1239.
Zhu, C.Y., Zhao, G.C., Sun, M., Liu, Q., Han, Y.G., Hou, W., Zhang, X.R., and Eizenhofer, P.R., 2015. Geochronology and geochemistry of the Yilan blueschists in the Heilongjiang Complex, northeastern China and tectonic implications. Lithos, 216: 241–253.
Zhu, C.Y., Zhao, G.C., Ji, J.Q., Han, Y.G., Liu, Q., Eizenhöfer, P.R., Zhang, X.R., and Hou, W.Z., 2017. Subduction between the Jiamusi and Songliao blocks: Geological, geochronological and geochemical constraints from the Heilongjiang Complex. Lithos, 282–283: 128–144.
Zorin, Y.A., 1999. Geodynamics of the western part of the Mongolia-Okhotsk collisional belt, Trans-Baikal region (Russia) and Mongolia. Tectonophysics, 306(1): 33–56.

About the first author

DONG Yu, female; born in 1990 in Changchun City, Jilin Province; doctor; graduated from Jilin University; postdoc of the College of Earth Sciences, Jilin University; she is now interested in the study on geochemistry. Email: dongyu1990@jlu.edu.cn; Tel: 18186893335.

About the corresponding author

GE Wenchun, male, born in 1963 in Fujin City, Heilongjiang Province; doctor; graduated from Changchun University of Technology; professor of the College of Earth Sciences, Jilin University; he is now interested in the study on petrology. Email: gewenchun@jlu.edu.cn; Tel: 13844058722.